A Novel Digital Hadron Calorimeter:

Analysis and Calibration with Muons

Daniel Trojand

Master of Science

Department of Physics

McGill University

Montreal, Quebec

April 3rd, 2012

A thesis submitted to McGill University in partial fulfillment of the

requirements of the M.Sc. degree

ACKNOWLEDGMENTS

I would like to thank my family for their continuous support in my ventures as a graduate student. I'd like to thank my friends and roommates for helping me push through the difficult parts and helping me stay focused. Without all of their support this task would have been extremely difficult. Finally, I would like to thank both of my supervisors, Dr. Francois Corriveau and Dr. Jose Repond for putting up with me and helping me with any problem I had.

Abstract

This thesis is a report on the design, construction and data analysis of the Digital Hadron Calorimeter (DHCAL). The DHCAL was constructed as part of the CALICE collaboration efforts in the SiD detector design for the proposed International Linear Collider (ILC). The SiD detector design is one of two detector designs for the ILC. The DHCAL is but one of the detector sub-systems that are to make up the entire detector. The CALICE collaboration is involved in the development of calorimeters for the ILC. The DHCAL utilizes Resistive Plate Chamber technology to detect the physics events and is the world's first digital imaging calorimeter. The prototype construction was performed at Argonne National Laboratory and the detector studied locally in a cosmic ray test stand. In addition, the DHCAL was also put into multiple test beam runs at Fermi National Accelerator Laboratory. This work will be completed with the analysis of the DHCAL data with muons. The calibration with muons will be discussed, as well as its purpose to the overall viability of this technology in a full scale detector.

Abrégé

Cette thèse est un rapport sur la conception, la construction et l'analyse des données du calorimètre hadronique digital (CALHD). Le CALHD a été construit dans le cadre des efforts menés par la collaboration CALICE pour la conception du détecteur SiD destiné au future Collisionneur Linéaire International (CLI). Le SiD est un des deux détecteurs proposés pour le CLI. Le CALHD lui-même n'est qu'un des sous-systèmes devant constituer le détecteur complet. La collaboration CALICE est impliquée dans le développement des calorimètres pour le CLI. Le CALHD utilise la technologie des chambers à plaques résistives pour détecter les événements physiques et est le premier calorimètre par images digitales au monde. La construction du prototype a été realisée au Laboratoire National Argonne et ses performances étudiées dans un montage de tests avec des rayons cosmiques. De plus, le CALHD a été placé à plusieurs reprises dans une ligne de fasiceau de particules au Laboratoire National d'Accélérateur Fermi. Ce travail sera complété par l'analyse des données du CALHD avec des muons. La calibration à l'aide de muons sera discutée, ainsi que la viabilité globale de cette technologie pour un détecteur à grande échelle.

TABLE OF CONTENTS

LIST OF TABLES

LIST OF FIGURES

1 Introduction

This thesis is a report on the design, construction and data analysis of the Digital Hadron Calorimeter (DHCAL) at Argonne National Laboratory and Fermi National Accelerator Laboratory. The DHCAL was constructed as part of the Calorimeter for ILC (CALICE) collaboration efforts in the Silicon Detector (SiD) design for the proposed International Linear Collider (ILC) – an electron-positron collider. The SiD detector design is one of two detector designs for the ILC. Figure 1.1 shows a quadrant view of the SiD design [1].

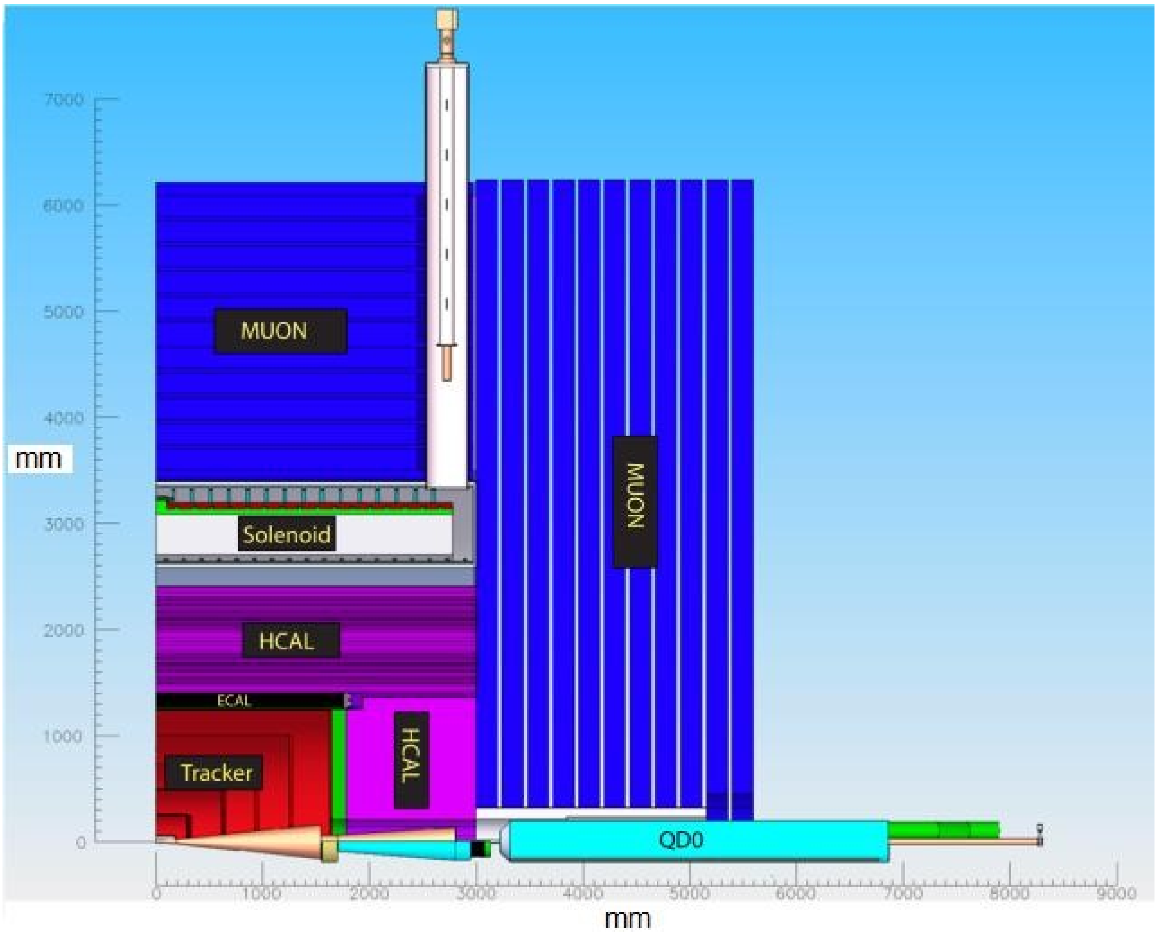

Figure 1.1: Quadrant view of the SiD detector design where the x-axis is parallel to the beam line and illustrates the size of each detector sub-system in order from closest to the interaction region: tracker, electromagnetic calorimeter, hadronic calorimeter, muon tracker. The y-axis is perpendicular to the beam line and illustrates the size of each detector sub-system in a radial direction in order from closest to the interaction region: tracker, electromagnetic calorimeter, hadronic calorimeter, solenoid magnet, muon tracker.

A hadron calorimeter is an important device used to measure the energy of impinging particles, most specifically neutral hadrons, since no other detector system is designed to measure them. Trackers measure the momenta of all charged particles, including the charged hadrons, with high precision while calorimeters will detect all types of particles except neutrinos, and so will be the only ones to measure the energy deposition of neutral hadrons. It is necessary to measure all the particles, including neutral hadrons, in order to understand what reaction occurred in the detector therefore each detector sub-system is crucial.

A brief discussion of the Standard Model of particle physics is presented in Chapter 2. The missing links still left in our understanding of the universe and how all elementary particles interact with each other is outlined. This is the physics to be studied at the Large Hadron Collider as well as the proposed International Linear Collider (ILC). A small introduction to the physics program at the ILC as well as details about the collider is given in Chapter 3.

The DHCAL is only one of the detector sub-systems that are to make up the entire detector. The details of calorimetry, how to detect the various particle species and the application of particle flow algorithms will be discussed in Chapter 4. This thesis work is done in conjunction with the CALICE collaboration and their involvement will be further discussed in chapter 5. The DHCAL utilizes Resistive Plate Chamber technology to detect the physics events and is the world's first digital imaging calorimeter. The DHCAL is so unique because of its small lateral and longitudinal granularity, and it is designed to be used with particle flow algorithms. These qualities are to be used to achieve unprecedented jet energy resolution. This is where my own work fully starts.

The construction was performed at Argonne National Laboratory and the detector studied locally in a cosmic ray test stand. In addition, the DHCAL was also put into multiple test beam runs at Fermi National Accelerator Laboratory which will be discussed in detail in chapter 6. This report concludes with the analysis of the DHCAL`s performance using a known muon source. The calibration with muons will be discussed in chapter 7, as well as the overall viability of the DHCAL in a full scale detector. A discussion of the results can be found in chapter 8.

2 Theory

It has been a long time since humanity has started thinking about everything we can see, and the theories have been ever changing. These theories started with the Greek philosopher Empedocles (490-430 B.C.) and his theory that matter is made of four basic elements; fire, air, water, and earth. The current theory of the fundamental elements in nature is the Standard Model (SM) of particle physics. This theory is very successful at explaining what the fundamental particles are and how they interact with each other. The SM has some predictive power, for example it predicted the existence of the top quark which was then found experimentally. This chapter is dedicated to exploring the world's currently accepted theory.

2.1 The Standard Model

The Standard Model (SM) breaks the elementary particles up into two categories based on an intrinsic property called spin. Particles whose spin value is an odd integer multiple of ½ are called Fermions and particles whose spin value is an even integer multiple of ½ are called Bosons. These bosons and fermions differ in which forces act on them and can be subdivided further into three different generations. Each generation of particles is heavier than the previous generation.

2.2 Fermions

The group of Fermions are broken down into two separate categories of particles called sectors which have different properties and are often involved in different types of interactions. These two sectors are the quarks and the leptons.

2.2.1 Quarks

Quarks come in six different flavours: up, down, charm, strange, top and bottom; a summary can be found in Table 2.1. The quarks have fractional charges of either of $2e/3$ or $-e/3$ (where 'e' is the electric charge of the proton, 1.602 x 10^{-19} C) and each has a different mass. Quarks have an additional quantum number which other elementary particles do not have, the color charge. There are three different color charges: blue, green, and red. There are six additional quarks which have the same mass as the regular quarks but have opposite quantum numbers and are referred to as anti-quarks. Quarks can only form color doublets or triplets, where the total color charge is neutral. An example of a colour doublet is a $u\bar{u}$ where the u has color red and $\bar{u}$ has color anti-red. Similarly, an example of a color triplet is a proton (quark content uud) where one u quark has a color charge of red, the other u quark has a color charge of blue and the d quark has a color charge of green. Quarks primarily interact via the strong force through the exchange of gluons (see section 2.3) but can also interact with any of the bosons [3].

Table 2.1: List of quarks and their charges.

Electric charge	First Generation	Second Generation	Third Generation
+2/3	*u* (up)	*c* (charm)	*t* (top)
-1/3	*d* (down)	*s* (strange)	*b* (bottom)

2.2.2 Leptons

There are six leptons which make up three generations similar to the quark sector. The leptons have electric charges of integer value, either zero or one. Each generation is more massive than the previous and consists of one massive charged particle and a very light neutrally charged particle called a neutrino. The first generation of leptons consists of the electron and the electron neutrino. The second generation of leptons consists of the muon and the muon neutrino. The third generation of leptons consists of the tau and the tau neutrino. Leptons are subject to all the fundamental forces except the strong force. Typical interactions involve the weak force through the exchange of W and Z bosons. The leptons have electric charge, spin and mass but do not have color charge. There are additionally six anti-leptons which have the same masses but differ in their quantum numbers from the regular leptons.

2.3 Gauge Bosons

Gauge bosons are responsible for the electromagnetic, weak and strong nuclear forces in the SM. It is important to note that the SM does not have a verified theory of gravity. Particles interact with each other via the exchange of a gauge boson. The photon is the gauge boson exchanged in electromagnetic interactions; it is a massless spin 1 particle. There are three massive bosons responsible for the weak nuclear force: W^+, W^-, and Z^0. The W's have unit charge, one positive and the other negative, while the Z is electrically neutral. The electromagnetic and weak forces have been unified into a single theory called the electroweak force. The last observed bosons are the gluons, of which there are eight different color/anti-color combinations. These particles interact with color charged particles, the quarks. Gluons are massless and because they have combination of color charges they can self interact.

The SM predicts another boson which has not yet been observed, the Higgs boson. In the electroweak theory the Higgs generates three Goldstone bosons and their masses. The last degree of freedom is used for the Higgs particle itself, with $J^{PC} = 0^{++}$. The masses of the quarks and leptons are generated through the Yukawa interaction with the Higgs field. Without the Higgs field, none of the particles in the SM would have any mass [5]. A summary of the particles with their properties can be seen in Figure 2.1 [6].

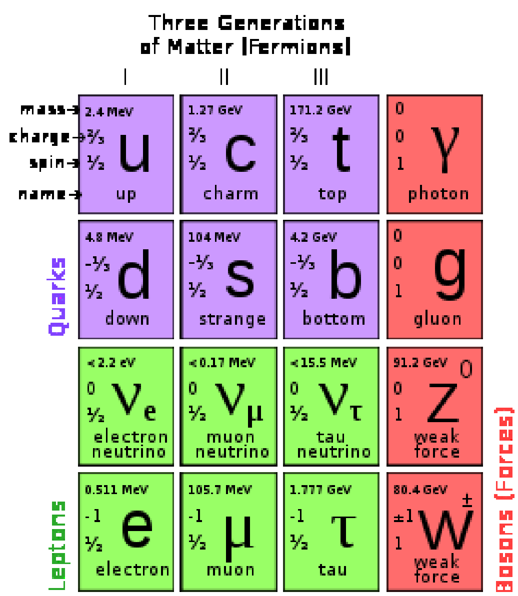

Figure 2.1: Elementary particles with their corresponding masses, charges, spins and names.

2.4 Shortcomings of the Standard Model

The SM is very successful and is a very useful theory for physicists; however there are some areas in which it gives no insight or predictions. The following topics are experimental observations that have no explanation from the SM and SM predications that have not yet been observed.

The SM is not able to unify all the forces. It has been speculated that all fundamental interactions are just different manifestations of the same unified interaction. Currently it is expected that at energies of 10^{16} GeV the strong, weak and electromagnetic coupling constants will be nearly equal to each other [7].

The Higgs boson is the only elementary particles of the SM which has not yet been experimentally observed.

The SM fails to include gravity which has been described by Einstein's theory of general relativity. The gravitational forces in particle physics reactions are in general very weak and can be ignored, but at the Planck scale they are theorized to become as strong as the other interactions and should be included in the SM.

The SM offers no explanation for the matter anti-matter asymmetry in the universe. With current theories of the Big Bang there should have been equal amounts of matter and anti-matter created and there is a clear abundance of matter in our universe. CP violation of neutral kaons explains part of the asymmetry but is not a strong enough mechanism to explain the current ratio of matter to anti-matter.

Dark matter has been observed cosmologically in several different ways; however, the SM has no dark matter candidate. Dark matter was first observed by Zwicky in 1933 while studying the Coma cluster of galaxies, he found there to be approximately 400 times more mass than predicted [8]. Dark matter does not interact with electromagnetic radiation and this gives rise to its name. There is no concrete understanding of dark matter yet and no direct evidence of its existence.

A new experiment equipped with a detector that has a very high energy resolution will be able to shed light on to the various topics in particle physics. Arguably the topic of most interest is currently the speculated existence of the Higgs boson and therefore more attention will be spent on being able to measure processes which will involve the Higgs boson. This is currently underway at the

Large Hadron Collider. A more focused search for the Higgs boson is planned at the ILC.

3 International Linear Collider

The ILC is a linear electron-positron collider with a tuneable center-of-mass energy ranging from 200 GeV to 500 GeV with an optional upgrade to 1 TeV. It has the added capability of running at the Z mass of 91 GeV/c^2. The particles are to be accelerated using superconducting radio frequency (RF) cavities with an accelerating gradient of 31.5 MV/m. The luminosity (the number of particles that cross a unit of area in a unit of time) of the ILC is proposed to be 2 x 10^{34} $cm^{-2}s^{-1}$ [9].

3.1 Machine Layout

The details of the machine layout are taken from the Reference Design Report which was released in 2007 and therefore are subject to change in the future [9]. A layout of the machine can be seen in Figure 3.1, and is comprised of several components: an electron source, a positron source, damping rings with a circumference of 6.7 km, beam transport from the damping rings to the linear accelerators, bunch compressor systems, two main linear accelerators each 11.3 km long, and two beam delivery systems to deliver the beams to the interaction point, each being 2.25 km long.

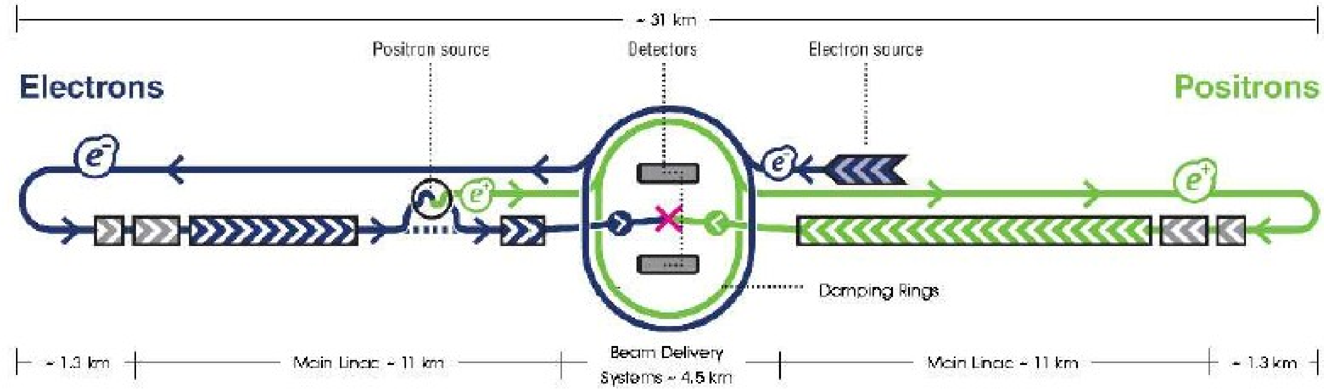

Figure 3.1: Layout of the proposed International Linear Collider.

3.2 Physics Program

The physics to be studied at the ILC is only partially dependent on the discoveries made at the Large Hadron Collider (LHC). The ILC is more of a precision machine than the LHC, in that the colliding particles at the ILC are fundamental particles (leptons) and have collisions with “cleaner” final states. The fundamental questions which are to be addressed are:

- What mechanism is responsible for the electroweak symmetry breaking and its generation of mass?

-How do the forces of nature unify?

-Does the structure of space-time at small distances show evidence of extra dimensions?

-What are the connections between the fundamental particles and forces and cosmology?

These questions are to be answered with the study of the Higgs boson properties, gauge boson properties, effects resulting from the existence of extra dimensions, supersymmetric particles, and the top quark properties. The studies of the Higgs boson intend to check the consistency of its properties with the SM, in particular: the Higgs' mass, width, branching ratios, couplings, and self coupling. It is expected, within the estimated precision of these measurements, that competing theories for electroweak symmetry breaking and generation of mass should be distinguishable. A wide range of models can be tested via the decay-independent detection of Higgstrahlung ($e^+e^- \rightarrow HZ$) events by Z tagging. If it turns out that there are no Higgs bosons, this scenario is addressed with the study of the coupling of gauge bosons. If there are additional Higgs bosons beyond the SM then they will also be studied at the ILC as long as their masses are within the scope of the ILC. The energy reach of the proposed detector is approximately 3 TeV in Higgs-less strong coupling scenarios (this energy range is due to potential upgrades of the ILC). In the case that supersymmetric particles are produced at the ILC, their masses and couplings can be measured which will allow a study of how the fundamental forces change with energy and how the forces unify at very high energies. These models include the models with strongly interacting W and Z bosons, and in some cases models with extra dimensions.

Further measurements of the top quark mass and its Yukawa coupling are to be performed [2].

4 Calorimeters

A calorimeter is an instrument that measures the energy deposited of particles in transit in order to determine their original energy. There are two different classifications of calorimeters in particle physics: homogeneous and sampling. A homogeneous calorimeter has no passive portion and the entire volume contributes to generate a signal. A sampling calorimeter consists of alternating layers of active and passive media. The active medium is used to generate a signal and the passive medium is used to absorb energy from the traversing particle to induce a particle shower, thus reducing the size and cost at the expense of detecting only a fraction of the energy deposited. Particles travelling through matter can interact with the nucleus or electrons/electric field of the atoms in the material. Understanding how these particles interact is fundamental to understanding how a calorimeter works and is to be used. This section will discuss the fundamental processes which take place in particle showers. This will be followed by a novel way to measure particle showers using particle flow algorithms (PFAs). How PFAs work will be described and the ensuing physical specifications for the detector hardware will be discussed.

4.1 Interactions of electrons with matter

A charged particle traversing a medium may be accelerated and/or scattered by the electric field of an atomic nucleus which will cause electromagnetic radiation called Bremsstrahlung. Bremsstrahlung is the main process for energy loss of highly energetic electrons and positrons. It is one of the processes responsible for electromagnetic showers. The average energy loss 'dE' per path length 'dx' from Bremsstrahlung is given empirically by [10]

$$-\frac{dE}{dx_{brems}} = 4\alpha\left(\frac{e^2}{Mc^2}\right)^2\left(\frac{N_A Z^2}{A}\right)z^2 E\ln\left(\frac{183}{Z^{1/3}}\right)$$

where 'Z' is the atomic number, 'A' is the atomic mass of the material, 'z' is the charge of the traversing particle, 'E' is the energy of the particle, 'M' is the mass of the incident particle, 'N_A' is Avogadro's number, and 'α' is the fine structure constant. A second process by which a charged particle traversing matter can interact is ionization of the target material. Ionization typically happens at lower energies and a plot of the different types of interactions of electrons and positrons can be seen in Figure 4.1 [11]. The curve indicated as MØller refers to MØller scattering or electron-electron scattering. The curve indicated as Bhabha scattering refers to electron-positron scattering.

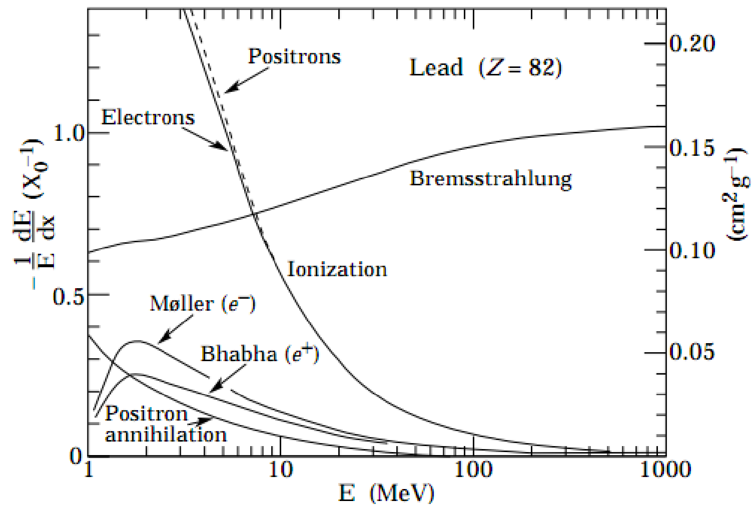

Figure 4.1: Stopping power as a function of energy for electrons and positrons in lead.

The typical length scale which an electron or positron must travel through matter before undergoing such a process is called the radiation length, X_0, usually measured in units g cm^{-2}. This length typically corresponds to the mean distance over which a highly energetic electron loses all but 1/e of its energy by Bremsstrahlung and 7/9 of the mean free path for pair production by a high energy photon. The mean free path can be calculated with the following equation [12].

$$X_0 = \frac{716.4 g cm^{-2} A}{Z(Z+1)\ln\left(287/\sqrt{Z}\right)}$$

4.2 Interactions of photons with matter

Unlike the electron/positron, the photon does not lose its energy in matter due to ionization or Bremsstrahlung. Photons traversing matter lose their energy primarily due to three electromagnetic processes: the photoelectric effect, Compton scattering, and pair production. Figure 4.2 shows the cross sections for the various processes at different energies [13]. At high energies, the dominant energy loss process is pair production and is the most important process for calorimetry.

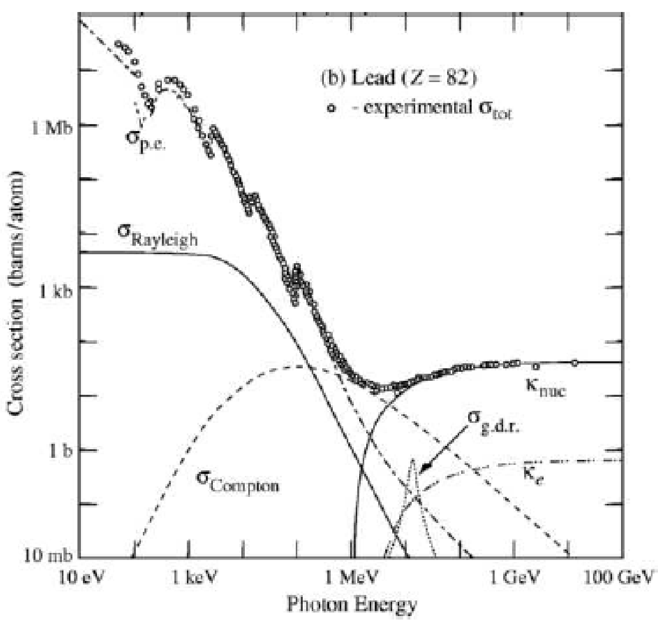

Figure 4.2: Photon cross section in barns/atom for the various processes for energies from 10 eV to 100 GeV.

The typical pair production interaction in matter is as follows

$$\gamma + nucleus \rightarrow e^+ + e^- + nucleus.$$

4.3 Interactions of muons with matter

This section is of special interest as muon data are the primary focus of this thesis. This section will go through the interactions of muons with matter. When a muon traverses matter there can be two primary outcomes: it can lose energy via excitations of atomic electrons and ionization, and it can be deflected. There are other processes which can cause such effects however these are the dominant processes in calorimetry. The mean rate of energy loss by heavy charged particles (muons fall into this category) is described by the Bethe-Bloch equation [14],

$$-\left\langle \frac{dE}{dx} \right\rangle = Kz^2 \frac{Z}{A\beta^2}\left[\frac{1}{2}\ln\frac{2m_e c^2 \beta^2 \gamma^2 T_{\max}}{I^2} - \beta^2 - \frac{\delta(\beta\gamma)}{2}\right]$$

where K/A = 0.31 MeV g^{-1} cm^2, 'T_{max}' is the maximum kinetic energy that can be transferred to an electron in a single collision, 'I' is the mean excitation energy of the material being traversed, 'δ(βγ)' is a density effect correction to ionization energy loss, β = v/c, $\gamma = \frac{1}{\sqrt{1-\beta^2}}$, and v is the speed of the particle.

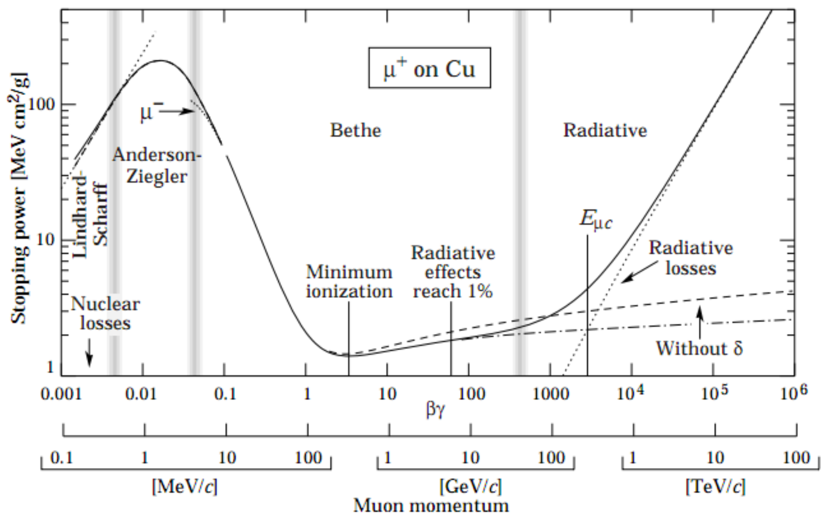

Figure 4.3: Stopping power as a function of energy for muons in copper.

The stopping power as a function of muon momentum is plotted for positive muons traversing copper in Figure 4.3 [15]. As the momentum increases the stopping power reaches a minimum of approximately 1.5 MeV cm^2/g, particles around this region are generally referred to as minimum ionizing particles or mips.

4.4 Interactions of hadrons with matter

This section will discuss the interactions of hadrons with matter, specifically: neutrons, protons and pions.

4.4.1 Interactions of neutrons with matter.

Neutrons interact with matter through different processes than previously described since they are neutrally charged fermions. As in all interactions with matter, the energy of the particle is crucial as to which process is more likely to occur. Neutrons can interact with matter through diffraction, elastic scattering, radiative capture, small nuclei capture, inelastic scattering, and nuclear fission. All such processes involve the interaction of a neutron with a nucleus. For the energies at which we are concerned, the inelastic and elastic scatterings are the only two important processes. Neutron scattering refers to processes in which a neutron interacts with a nucleus, or when the neutron breaks up the nucleus into fragments such as light nuclei and protons or further neutrons which will interact in the calorimeter provided they have sufficient energy. The neutron can also excite the nucleus in which it loses some of its energy and the nucleus will later radiate a photon when it de-excites.

4.4.2 Interactions of protons with matter

Protons interact similarly to muons in that they will lose energy due to ionization and leave “tracks” through the calorimeter. They differ in that they can interact via the strong force to produce a cascade of secondary particles. They can scatter inelastically with nuclei in which they break up nuclei or excite a nucleus just as neutrons do.

4.4.3 Interactions of pions with matter

Charged pions interact similarly to muons and protons in that they interact electromagnetically (via ionization) to leave tracks in the calorimeter. In addition they can interact via the strong force with nuclei to break up or excite the nuclei similarly to the neutron or proton interactions. The charged pion can further interact through the weak force to produce a muon and a muon neutrino. The muon neutrino will not be seen at all by the calorimeter. The neutral pion decays electromagnetically as well to produce two photons (other decays products are possible but highly unlikely).

4.5 Electromagnetic showers

An electromagnetic shower starts with a highly energetic electron, positron, or photon traversing matter. The initial particle then interacts with the matter most likely via pair production if the initial particle is a photon, or via Bremsstrahlung if the initial particle is an electron/positron (ionization also occurs for the leptons). The daughter particles will continue to interact with the matter via pair production and Bremsstrahlung until the particles do not have enough energy for either. A simple model of how an electromagnetic shower occurs will be discussed and its important properties calculated. A deep understanding of electromagnetic showers is integral in understanding hadronic showers and thus it is reported in detail here.

4.5.1 Shower models

To get a physical picture of an electromagnetic shower we can look at a simple shower model (see Figure 4.4 [16]). One can model an electromagnetic shower by using four simple assumptions.

- An electron above critical energy (see section 4.5.2) will travel one radiation length before it gives up 1/e its energy to a Bremsstrahlung photon.
- A photon above critical energy will travel one radiation length before it undergoes pair production and gives each particle half of its energy.
- Electrons below the critical energy will stop radiating and lose the rest of their energies due to collisions/ionizations.
- For electrons above the critical energy we will neglect ionization losses.

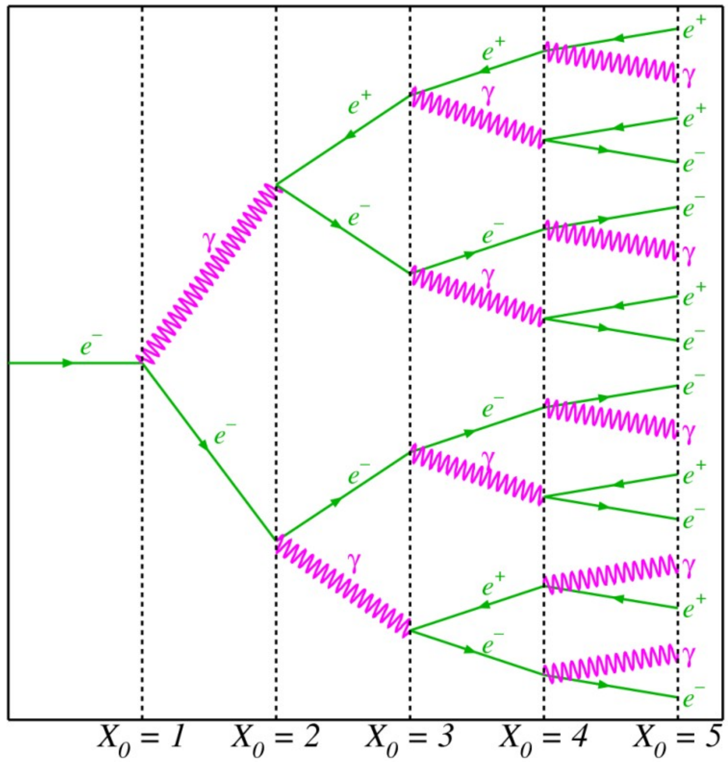

Figure 4.4: Electromagnetic shower due to an incident electron according to the simple shower model, where X_0 is the radiation length of the media.

There are several models that can be used in order to understand electromagnetic showers or to model them for simulation. The above simple shower model is used as a toy model to get a better physical understanding of what is going on but it does not work well in practice. The most successful modeling software is EGS4 [17], which is a Monte Carlo based software and can handle almost any electron-photon transport problem. In addition, what makes

EGS4 work so well is that it does not neglect the low energy processes (ignored in the simple shower model) and it uses a real representation of the detector.

4.5.2 Longitudinal development

The distance the shower will reach in the detector plays a major role in the design and the physical dimensions of the detector. Ability to calculate such quantities is crucial in the design phase of the experiment. In order to make some of the equations simpler we will introduce two new variables which will make things seemingly material independent. The first variable is $t = x/X_0$ where 'x' is the distance travelled by the particle in the detector and 'X_0' is the radiation length of the material. The second variable is $y = E/E_c$ where 'E' is the particle's energy and 'E_c' is the critical energy. The critical energy is the point at which the collision loss rate is equal to the Bremsstrahlung loss rate and can be calculated with the following equation [18]

$$E_c = (800MeV)/(Z + 1.2)$$

The longitudinal profile of an electromagnetic shower is well described by the following function

$$\frac{dE}{dt} = E_0 b \frac{(bt)^{a-1} e^{-bt}}{\Gamma(a)}$$

where the variables 'a' and 'b' can be readily solved using the previous equations along with the following equation

$$t_{\max} = (a-1)/b = 1.0 \times (\ln y + C_j), j = e, \gamma, C_e = -0.5, C_\gamma = 0.5$$

't_{max}' is the distance at which the shower reaches the greatest number of particles before tapering off [19].

4.5.3 Lateral development

An electromagnetic shower will increase in size radially as the shower progresses and then decrease after the shower maximum is reached. The increase in width is due to secondary electrons and photons which are not aligned with the incident particle. Processes such as Coulomb and Compton scattering will produce more particles which will not follow the incident particle's trajectory and will in turn produce more particles and extend the cascade. One variable which is used to well describe the width of electromagnetic showers is the Molière radius. The Molière radius for a given material is defined by the following equation $R_M = X_0 E_s / E_c$, where $E_s \approx 21$ MeV [20]. The Molière radius for a compound material is given by the equation $\frac{1}{R_M} = \frac{1}{E_s} \sum_i \frac{w_i E_{ci}}{X_i}$ where w_i is the weight fraction of the element with critical energy E_{ci} and radiation length X_i [20,21]. Experimental data has shown that on average 90% of the energy of an electromagnetic shower is contained in a cylinder whose radius is 1 R_M. In a cylinder with a radius of 2 R_M, it is said that 95% of the energy is contained. The distribution of the width can be represented with the following equation

$$f(r) = \frac{2rR^2}{\left(r^2 + R^2\right)^2}$$

where, R is a free parameter which can be fitted with data [22].

4.6 Hadronic Showers

Analogously to the electromagnetic showers, hadronic shower has the same shower properties that are of interest: longitudinal and lateral shower development. There is no complete theory to describe hadronic showers as there is with electromagnetic showers. There are no simple models to use as analogies as in the case of the electromagnetic showers.

Hadronic showers are generated by the inelastic interactions of hadrons. When these processes happen in succession they produce a cascade of particles. In the energy regime dealt with in test beam runs (1-120 GeV) and collider environments these interactions are typically multiple particle production, particle emission from particle decay or nuclear excitations. Neutral pions are very often produced in these interactions and their main decay chain is into two photons which give rise to an electromagnetic component. For this reason it is important we understand electromagnetic showers (see section 4.5).

The shower properties are best described in terms of a variable called the nuclear interaction length which is analogous to the radiation length for electromagnetic interactions; it is the mean free path distance a particle travels before it interacts in a given material. The nuclear interaction length is defined by the following equation [23]

$$\lambda_i = \frac{Z}{N_A \rho \sigma_{nA}} \approx 35 \frac{A^{1/3}}{\rho} cm$$

where 'Z' is the atomic number, 'A' is the atomic mass of the material, 'ρ' is the density of the material, 'N_A' is Avogadro's number, and 'σ_{nA}' is the cross section. The length at which a hadronic shower develops before the energy deposition starts to taper off can be parameterized by the following equation

$$l_{\max} \approx [0.6\log(E) - 0.2]\lambda_i$$

where 'E' is the energy of the initial particle in units of GeV [23]. It is often referred to as the shower maximum, after which the longitudinal shower profile will decay exponentially until all the energy is deposited or has leaked out of the calorimeter. The exponential shape is not precisely known and differs for different particle energies, species, and material. The full depth at which 95% of a hadronic shower is contained can be parameterized by [23]

$$l_{95\%} \approx l_{\max} + 4E^{0.15}\lambda_i$$

A final parameter that has been investigated previously is the shower radius, specifically the radius which contains 95% of the shower radially. A rough equation for the 95% containment radius is as follows

$$R_{95\%} \approx \lambda_i$$

4.7 Particle Flow Algorithm

Particle Flow Algorithms (PFAs) are a new approach for processing the data from large particle physics detectors. One of the main current limitations we have on reconstructing certain interactions is the jet energy resolution. A jet is similar to a particle shower in that it starts a cascade of particles but differs in the way that it is initiated. A jet is initiated from a highly energetic quark or gluon which then interacts with the surrounding media to produce hadrons which can then produce particle showers which will be measured by the calorimeter.

PFAs are of particular importance because they can potentially improve the reconstructed jet energy resolution by a factor of two. This improved jet energy resolution will be used to disentangle the complex multi-jet final states expected to be seen at the ILC. The use of PFAs is new and still under development.

Traditionally in calorimetry all the energies of the jet would be measured with the electromagnetic calorimeter (ECAL) and hadronic calorimeter (HCAL); typically 70% of that energy would be measured in the HCAL alone. The calorimeter is typically the detector sub-system with the worst energy resolution and therefore a poor candidate to have to use to measure a large fraction of the shower energy.

The concept of PFAs is to use all of the information at hand from each part of the detector to get the best possible resolution. PFA requires the reconstruction of the four-vectors of all visible particles in an event. In a typical jet 60% of the deposited energy is due to charged hadrons, 30% is due to photons and the remaining 10% is from neutral hadrons. In this regime the charged particles will be reconstructed with the tracker, the photons will be reconstructed with the ECAL and the neutral particles will be reconstructed with the ECAL and HCAL. By lowering the percentage of energy measured with the HCAL PFAs inherently improve the total jet energy resolution. The most important and difficult part of using PFAs is to assign correctly the calorimeter hits to the correct particles in neighbouring showers [24]. This will be further discussed in section 4.8.

4.8 Detector Requirements for Particle Flow Algorithms

Calorimeters have not previously been designed to work with PFAs. In order for PFAs to work properly the detector must have certain characteristics. The PFA approach is not just an algorithmic approach or a detector design approach but rather both. The hardware requirements, strictly speaking the hadronic calorimeter requirements needed to utilize this approach are centered on it being a highly granular segmentation scheme both laterally and longitudinally. The jet energy resolution required to best measure the physics at the ILC is $\Delta E / E \approx 3-4\%$. The trackers momentum resolution for required charged particles is $\Delta p_i / p_i = 5x10^{-5}$. Table 4.1 [25] shows in more detail which physics process is to be measured with the corresponding detector sub-system requirement.

Table 4.1:

Physics Process	Measure Quantity	Critical System	Required Performance
ZHH $HZ \to q\bar{q}b\bar{b}$ $ZH \to ZWW*$ $\nu\bar{\nu}W^+W^-$	Triple Higgs Coupling Higgs Mass $B(H \to WW*)$ $\sigma(e^+e^- \to \nu\bar{\nu}W^+W^-)$	Calorimeter (and Tracker)	3 to 4%
$ZH \to l^+l^-X$ $\mu^+\mu^-(\gamma)$ $ZH + H\nu\nu \to \mu^+\mu^-X$	Higgs Recoil Mass Luminosity Weighted E_{cm} $B(H \to \mu^+\mu^-)$	Tracker	5 x 10^{-5}
$HZ, H \to b\bar{b}, c\bar{c}, gg$ $b\bar{b}$	Higgs Branching Fractions B quark charge asymmetry	Vertex Detector	$5\mu m \oplus 10\mu m / p(GeV/c)\sin^{3/2}\theta$
SUSY, eg. $\tilde{\mu}$ decay	$\tilde{\mu}$ mass	Tracker Calorimeter	

5 CALICE

The CALICE collaboration is an effort of scientists and engineers from various institutions and laboratories around the world to design a calorimeter for the next lepton-lepton collider ILC at the TeV energy scale [26]. It is to be a high granularity calorimeter system which will be optimised for particle flow measurements (see section 4.7) of multi-jet final states. As proof of concept, CALICE intends to show that high calorimeter performances can be achieved and that simulations can reproduce the measurements gathered from several test beam periods. The collaboration has developed various prototypes for each of the calorimeter subsystems: electromagnetic calorimeters (ECAL), hadronic calorimeters (HCAL), and tail catcher/muon tracker (TCMT). The work of this thesis is centered on the construction and testing of a physics prototype Digital Hadron Calorimeter (DHCAL) equipped with resistive plate chambers as active medium. An overview of the other completed physics prototypes will be given.

5.1 Electromagnetic Calorimeter

The Electromagnetic Calorimeter (ECAL) is a sampling calorimeter built from tungsten and silicon. Tungsten is used for the absorber due to its small Molière radius of 0.9 cm and small radiation length of 0.35 cm. The sensors are 500 μm thick and segmented into 1 x 1 cm^2 pixels. The ECAL is 24 radiation lengths deep and split into 30 absorber layers interleaved with sensitive silicon layers. The longitudinal segmentation is achieved through three regions of 0.14 cm, 0.28 cm and 0.42 cm thick tungsten absorbers. The silicon layers have an active area of 18 x 18 cm^2 [27].

5.2 Analogue Hadron Calorimeter

The Analogue Hadron Calorimeter (AHCAL) is a 1 m^3 sampling calorimeter utilizing plastic scintillators as active media with interleaved steel absorber plates. It consists of 38 scintillator tile layers measuring 90 x 90 cm^2, with a corresponding depth of 5 nuclear interaction lengths. To achieve high granularity each layer has one hundred 3 x 3 cm^2 tiles in the center, surrounded by 6 x 6 cm^2 tiles which themselves are surrounded by a strip of 12 x 12 cm^2 tiles. There are a total of 7608 tiles which are read out by wavelength shifting fibres which irradiate small silicon photomultipliers that are unaffected by magnetic fields [28].

5.3 Tail Catcher Muon Tracker

The TCMT is structured like a sampling calorimeter with an active medium of scintillator and passive medium of steel. There are a total of 16 absorber layers in the TCMT separated by 3.15 cm gaps interleaved with 0.95 cm thick readout modules. The first 8 layers are more finely segmented with a thickness of 1.9 cm and the last 8 layers are more coarsely segmented with a thickness of 10.2 cm. The read-out modules have a 100.0 x 100.0 x 0.5 cm^3 scintillator plane which is subdivided into twenty 100.0 x 5.0 cm^2 strips. The strips alternate between x and y orientations in adjacent layers to improve the position resolution [29].

5.4 Digital Hadron Calorimeter

The DHCAL is the basis of this thesis and will be explained in much greater detail in chapter 6.

6 Digital Hadron Calorimeter Design and Construction

The Digital Hadron Calorimeter (DHCAL) is a physics prototype hadron calorimeter designed and built at Argonne National Laboratory (ANL) utilizing Resistive Plate Chamber (RPC) technology in conjunction with the efforts of the CALICE collaboration.

6.1 Resistive plate chamber

The resistive plate chamber technology was created in the 1980's [30] and is being used again. The RPCs in the DHCAL are built from two parallel glass planes coated with high surface resistivity paint (1-10 MΩ/□, where □ is an area). The two pieces of glass have different thicknesses, the anode piece is 0.85 mm thick (thinner so that the readout signal is stronger) and the cathode piece is 1.15 mm thick. The gas gap in the RPCs is 1.15 mm in thickness and is filled with a 3 gas mixture (see section 6.5). The pieces of glass are placed in a PVC frame which has outside dimensions of 964.8 x 324.8 x 3.35 mm^3. The frames have an inside lip all the way around where the glass can make contact with the frame for gluing purposes. Fishing lines running parallel to the long side of the RPC are used as gas barriers and to keep the plates parallel. The fishing lines have a casing which does not run the entire length of the chamber but leaves an approximately 5 cm gap to allow gas to flow through. These gaps are staggered on either end of the chamber as in Figure 6.1 to force the gas to flush out of all areas of the chambers so that it is not depleted after several avalanches. The gas comes in from the bottom right and zigzags its way out at the top left side of the chamber. The RPCs are run in avalanche mode. An avalanche is initialized when a charged particle ionizes the molecules in the gas gap and then those free electrons are accelerated by the high voltage applied across the chamber which, then free more electrons and this process is repeated (see section 6.3 for more detail).

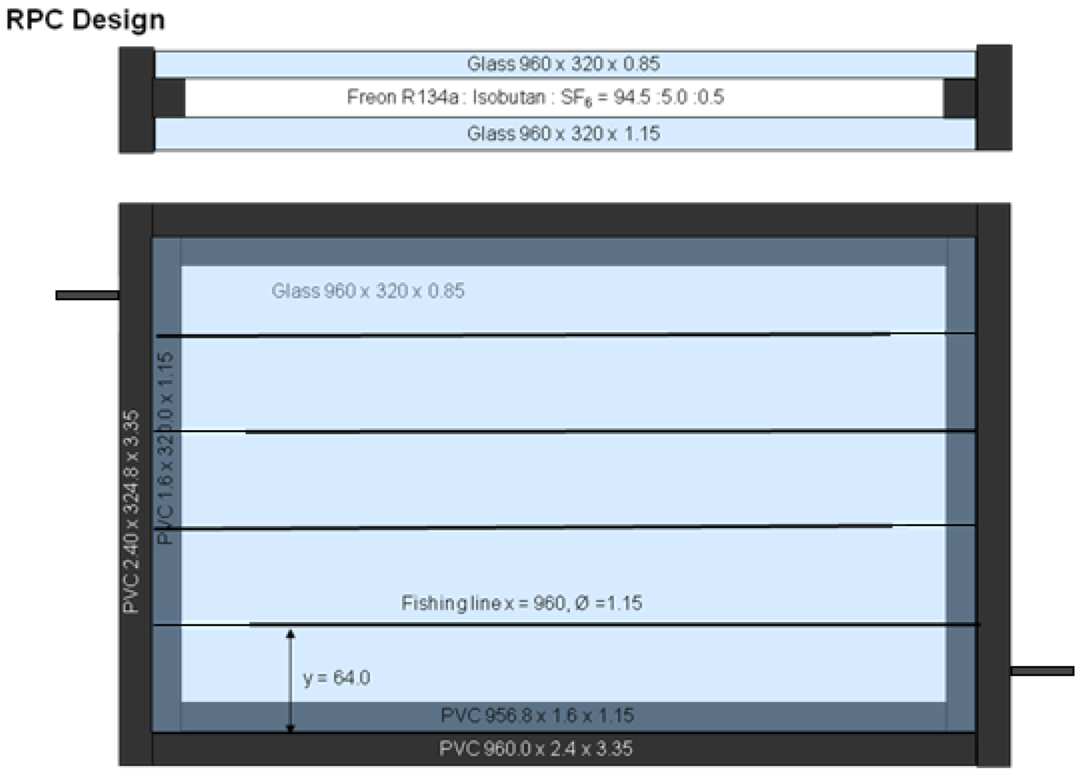

Figure 6.1: Schematic view of the top and side of an RPC where all measurements are in units of mm.

6.2 Front-end electronics boards

The electronic read-out system was designed jointly by ANL and FNAL, and has a pad size of 1 x 1 cm^2 and single bit resolution to satisfy the granularity required to utilize PFAs. Each RPC has two front-end electronics boards (FEBs) as the size required for on entire RPC was too difficult and expensive to manufacture as a single board. The front-end board electronics are very complex multilayered boards which, if produced as a single board would require blind and buried vias (vertical interconnect accesses) to make connections through multiple layers. It is necessary for these connections to end before the pad board connections as to not mix connections. It was therefore decided to have the pad boards made separately from the boards which housed the logic and this required the two boards to be glued together. Each front-end board is glued together with two different epoxies, a conductive epoxy for the pads and a non conductive epoxy for the rims and space between pads. A front-end board has 1536 channels each corresponding to a 1 x 1 cm^2 pad on a pad board. The FEBs house 24 application-specific integrated circuits (ASICs), DCAL III chips (see section 6.2.2), each of which have 64 channels corresponding to an 8 x 8 cm^2 area of the pad board. The pad board's measure 48 x 32 cm^2 and the FEBs measure 55.6 x 32 cm^2, the additional volume is occupied by the data concentrators and connectors for the low voltage cables (see Figure 6.2). The 24 ASICs are connected to the data concentrators, more about how the data is read-out will follow in section 6.6.3.

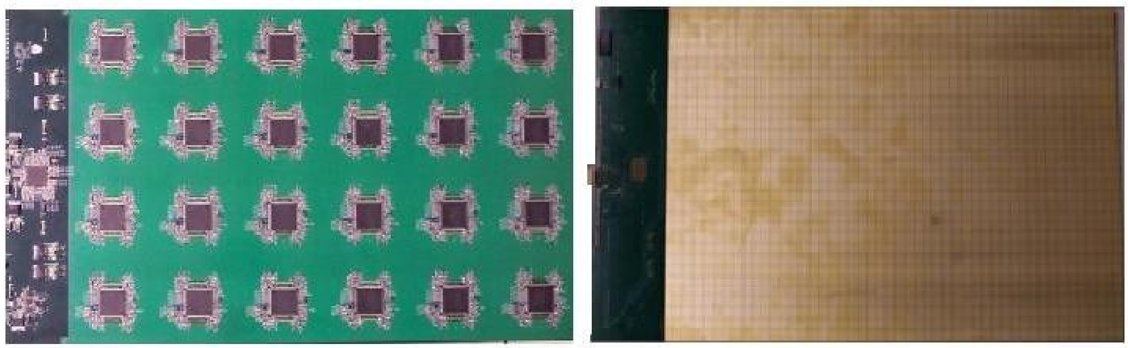

Figure 6.2: Top (left) and bottom (right) view of a completed FEB with its 24 ASIC integrated circuits, the left 4 cm section is where the data concentrator is located.

The FEB on the RPC structure is detailed in Figure 6.3. The FEBs are placed on top of the RPCs with a sheet of Mylar between them. The sheet of Mylar is placed between the pads and resistive paint so that the charge gets localized to a single pad on the pad board.

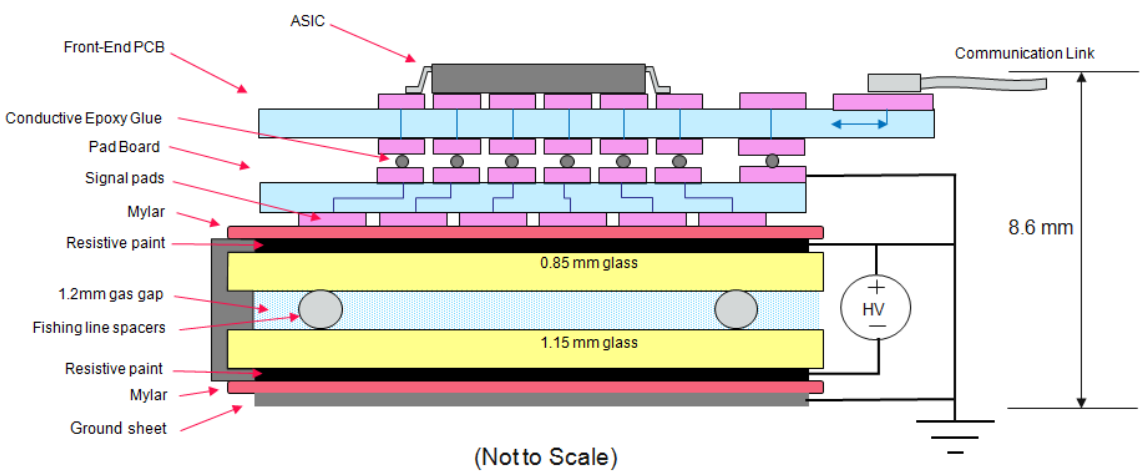

Figure 6.3: Physical details of the RPCs and FEBs on top of each other.

6.2.1 Gluing the front-end electronics boards

This is where my own work fully starts. A gluing device was built to automate the gluing process. The fixture has a flat surface parallel to the table where the FEB sits. The bottom surface has grooves cut out so that we can use a vacuum pump to create a pressure gradient to hold the board down while it is being glued. There are fixed pins on the fixture to align the FEB on the fixture and a mechanical arm able to move a syringe (filled with “!epoxy technology’s epo-tek e4110” epoxy) in the x and y plane to deposit glue. The fixture only glues the pads with the conductive epoxy. The inter-pad spaces are glued by hand using a curved tip syringe. After the gluing machine finishes putting the epoxy on the pads we put the pad board on another fixture to manually glue spacers (approximately 3 mm x 3 mm x 13 μm) in between the pads in an array (approximately 1 every 7 pads) over the board with “Loctite 430” instant adhesive to stop the epoxy from smearing and possibly connecting some of the channels together when pressure is applied to join the two boards. Using “3M Scotch-Weld Acrylic Adhesive DP-820” we then glue around the edges and in between every 3 columns of pads to firmly hold the pad board to the FEB. The FEB is then placed onto the pad board and covered with aluminum plates which have sunken areas to avoid putting pressure on the DCAL III chips. Weights are then placed on top of these aluminum plates. After approximately 15 minutes the boards along with the second fixture are put into an oven set to 70°C overnight to cure the epoxy. A total of 228 FEBs are required to fully equip the 38 layers of the DHCAL however a total of 324 were glued in case any of the FEBs malfunctioned (Note: 14 layers for the TCMT were later equipped with RPCs and required 42 FEBs).

6.2.2 DCAL III Chip

The readout is performed with the DCAL III chip which is jointly designed by ANL and FNAL. The DCAL III has a 64 channel readout which can operate in two gain ranges: high gain mode developed to run with Gas Electron Multipliers with a signal range of 10-200 fC, and low gain mode developed to run with RPCs with a signal range of 100 fC-10 pC. The DCAL III chips have a threshold set by an 8-bit DAC which is common for all 64 channels. The 8-bit DAC threshold range corresponds to a signal range of 0 fC to approximately 600 fC. There are two readout modes: triggered readout mode which is used for testing with cosmic rays and test beam runs, and triggerless readout mode which is used for performing noise measurements [31].

6.3 Resistive plate chamber signal production

The signal of impinging particles is seen by the electronics system as a charge pulse. The pulse is generated by an avalanche within the gas volume. If the initial particle is energetic enough to ionize the gas molecules in the gas volume then both electrons and ions will collide with the neutral gas molecules. If a strong enough electric field is applied across the gas gap then the electrons will gain enough kinetic energy to ionize other gas molecules. This process can continue and more ionization can occur, the process is called a Townsend avalanche. The applied electric field must be above a certain threshold to produce such a phenomenon. Additional details on the electron transport through the gas gap and glass can be found in [32].

The top piece of glass and pads of the FEBs have a potential difference between them so that the electrons will be accelerated into the pads. The electrons will travel through the conductive pads, generate a signal and this signal goes into an amplifier on the FEB. The electrons will create a measurable pulse which will then be analysed with the electronics on the FEBs.

6.4 Construction

The construction of the DHCAL at ANL had multiple stages and will be broken down in the next sections. The construction involved spraying and testing the glass for the RPCs, assembling the RPCs, gluing the FEBs, and assembling the cassettes.

6.4.1 Spraying

A conductive coating was put on one side of the glass so that a high voltage can be applied to the outside of the chamber. The conductive paint was sprayed on using an air brush (later a spray gun) in our custom built spray booth. The spray booth was automated such that a uniform layer of paint would cover the glass.

The spray booth was a three-walled structure with a roof. The open wall was partially covered with Mylar (from the ground up to ~ 48”) to keep the vapours of paint contained. The back wall had an exhaust fan behind an artificial wall of filters which removed paint fumes from the air. A motorized back plate was in the center of the booth which could be raised and lowered on two threaded bars. A rail which housed the arm for holding the spray gun was parallel to the ground at an elevation of ~48”. There were two limit switches on either end of the rail which told the program to stop the horizontal motion, move the plate vertically, and then move back along the rail running horizontally.

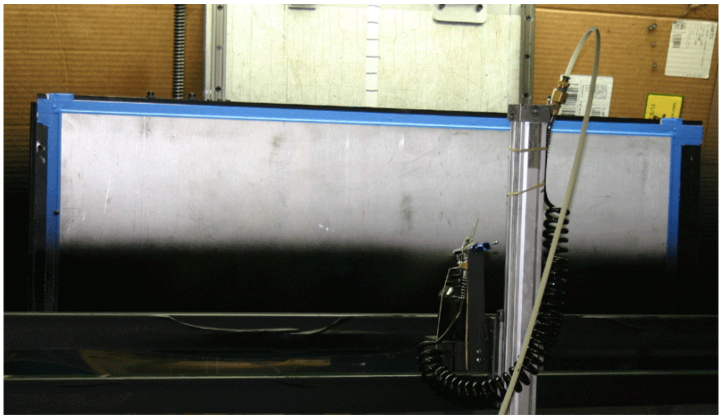

Figure 6.4: Photograph of a piece of glass being sprayed in the spray booth. The black portion is the painted part and the white portion is not painted.

The sheets of glass were taped to an aluminum plate which was then mounted to a back plate in the spray booth. The airbrush was fixed to an arm which moved back and forth horizontally (see Figure 6.4). The back plate in the spray booth lowered after each time the air brush made a pass (moved from the left side to the right side or vice versa). In this manner the sheet of glass got an even layer of paint deposited onto its surface. The desired surface resistivity was in the range of 1 – 10 MΩ/□ and we measured the surface resistivity of the glass with a 6 x 6 cm^2 probe with two parallel strips of copper on the outer edges which were connected with wires to an ohmmeter. We measured the resistivity and recorded the values in a checker board pattern over the entire sheet of glass (see Figure 6.5).

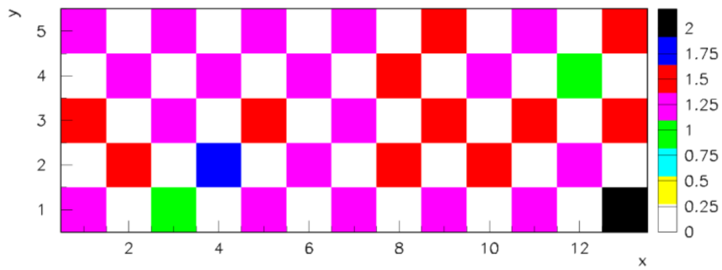

Figure 6.5: Surface resistivity measurements for a piece of glass, measured in a checker board pattern.

The paint was a mixture of two different paints bought from an outside manufacturer and water. The paints used were Badger Air Opaque chrome oxide “green 8.40” and “black 7-01”. The mixture contained 32.2% black paint, 30.3% green paint and 37.5% water. These ratios were determined by systematically trying different paint ratios and measuring the surface resistivity of the glass sheets. The airbrush used initially was from Central Pneumatic; the “Deluxe Air Brush Kit”*.* We opted to get a spray gun in order to increase reproducibility and increase production. With the old air brush we could spray 3 sheets of glass per day. This restriction was due to two factors, the width of spray, and the necessity to clean the air brush between the spraying of each sheet of glass. The new spray gun was highly adjustable and able to have a variety of widths and paint flow rates. The spray gun was the “Binks model 2100 spray gun” equipped with the needle and nozzle which gave the finest atomization of the paint. A maximum of 8 sheets of glass could be sprayed a day without having to disassemble the spray gun and clean it in between each sheet of glass. The limiting factor was the space to store the freshly painted sheets of glass since it took approximately 8 hours for the paint to dry completely.

The result of this work yielded approximately 650 pieces of glass being sprayed, 400 of which were acceptable. Occasionally a piece of glass was broken or chipped at the edge. Figure 6.6 shows the mean surface resistivity for each of the pieces of glass as a function of the glass number. The rejection criteria were based on the surface resistivity. The yellow band indicates which of the pieces were accepted.

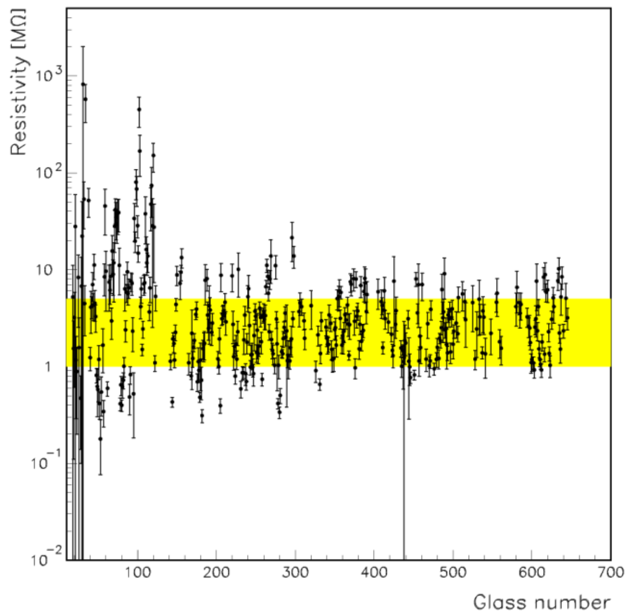

Figure 6.6: The surface resistivity of all the glass sprayed to make RPCs, where the yellow band indicates the accepted pieces of glass (surface resistivity between 1-5 MΩ/□).

There were fewer fluctuations in the surface resistivity as time went on as our experience with painting increased. The uniformity of the surface resistivity can be seen in Figure 6.7, where the RMS of each plate versus the mean resistivity is plotted for both thick and thin pieces of glass.

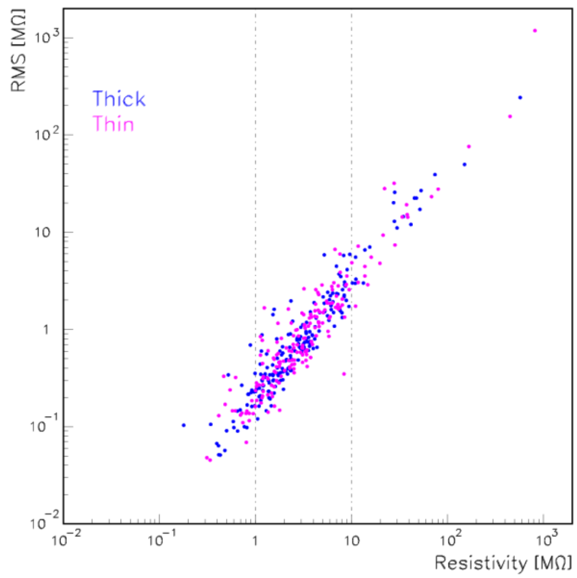

Figure 6.7: The root mean squared value of the surface resistivity as a function of the surface resistivity for thick and thin glass.

The RMS of the majority of the pieces of glass lied between 0.10 and 10 MΩ/□, some pieces outside of this range were used to make RPCs but most were within this limit.

In an experiment it is hoped that all variables were controlled; however, the painting process did not have this luxury. The environment inside the spray booth was not stable and was very sensitive to temperature and humidity changes outside. Due to the quantity of glass sprayed and the time it took there were many fluctuations due to the change of seasons. There were no environmental controls in the spray booth and as the temperature and/or humidity changed, our results changed. We adjusted the flow rate on the spray gun to compensate for the change and were not always successful. There was an added adversity; it was found that the viscosity of paint was not consistent between different bottles of paint, partially due to weather changes.

6.4.2 RPC assembly

The frames themselves were cut and glued together out of four cut pieces of PVC. Three custom fixtures built at ANL held the frame in place while the glue dried. The fixture was used for gluing the frame together, gluing the glass to the frame and installing the fishing line gas barriers. The frame was glued together and a thick piece of painted glass was glued into place. The glue was then allowed to dry overnight. The frame and glass were then flipped over to install the fishing lines. Then there were four nylon fishing lines installed, running parallel to the length of the chamber, with a plastic sleeve covering approximately 90% of the length of the line. The sleeves were staggered so that the gas would flow through the RPC to avoid stagnant gas molecules from accumulating (as described in section 6.1). The fishing lines were then tensioned and tied off. A thin piece of glass was glued into the frame. Then the gas inlet tubes and high voltage mounting fixtures were glued into place. The high voltage lines were then attached by connecting a piece of copper tape to the short side of the RPC which made contact with the paint on the glass. The strips of tape were roughly 4 cm long by 1 cm wide; the tape was placed on the RPC such that each glass plate had an area of 2 x 1 cm^2 covered with tape. This length of tape seemed to be adequate to maintain the high voltage between the parallel plates. The adhesive on the copper tape was conductive in order to transfer the high voltage (HV). A sheet of Mylar was taped on both sides of the chamber to insulate the RPC from the steel plates and FEBs in the cassettes.

6.4.2.1 Quality Assurance

The chambers were put through a series of tests to make sure that they were uniform in quality. The first test was a pressure test to check for leaks; the equivalent of 0.3 inches water column pressure was put through the chamber. The RPC passed the test if the pressure drop was less than 0.02 inches over a 30 s time interval.

The uniformity of the gas gap thickness was checked by measuring the thickness along the edges. The middle of the RPCs was kept uniform by the gas barriers and was therefore not measured. Figure 6.8 shows the results from one RPC, this was a typical result where the corners could be seen to be slightly thicker

(0.3-0.4 mm). This result was not enough to affect the efficiency of the RPCs: only approximately 3% RPCs were affected by this increased gap size.

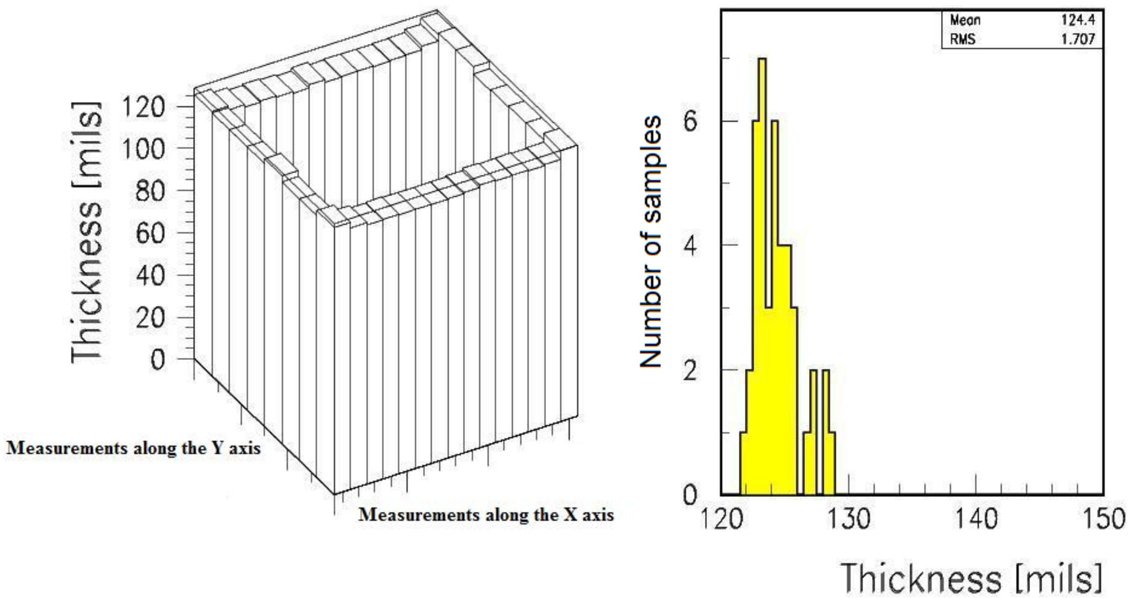

Figure 6.8: Thickness of the edge of an RPC shown geometrically (left) and in histogram form (right). Fifteen measurements were made along the X axis on each side and eight measurements along the Y axis on each side. 124 mils correspond to 3.15 mm which is exactly the gas gap plus the two plates of glass.

The RPCs high voltage operation was tested by applying a 7.0 kV potential for approximately 24 hours. During the test the RPCs were required to maintain a current of less than 0.3 μA. If the current spiked and the system tripped, then the RPC would not pass the test.

6.4.3 Cassette assembly

A cassette was a layer of three RPCs housed with the electronics between a sheet of copper and a sheet of steel. The copper sheets were 960.0 x 1003.0 x 2.0 mm^3 and had eight holes separated by 228.6 mm in the x dimension and 324.8 mm in the y dimension. The steel sheets were 960.0 x 998.0 x 2.0 mm^3 and had eight holes at the same place as the copper sheets. The copper sheet was slightly taller: the extra height is called a "fin" to stick up to be used as a heat sink. The holes in the sheets of metal were used to tension the cassette to keep it as compact and vertical as possible. The copper sheet was chosen for its ability to dissipate heat and was making contact with the ASICs to act as a heat sink.

A cassette had a copper bar attached at the top of the steel sheet and a steel bar at the bottom. Four badminton strings were placed through the eight holes in the steel sheet (see Figure 6.9) to hold all the layers in the cassette together.

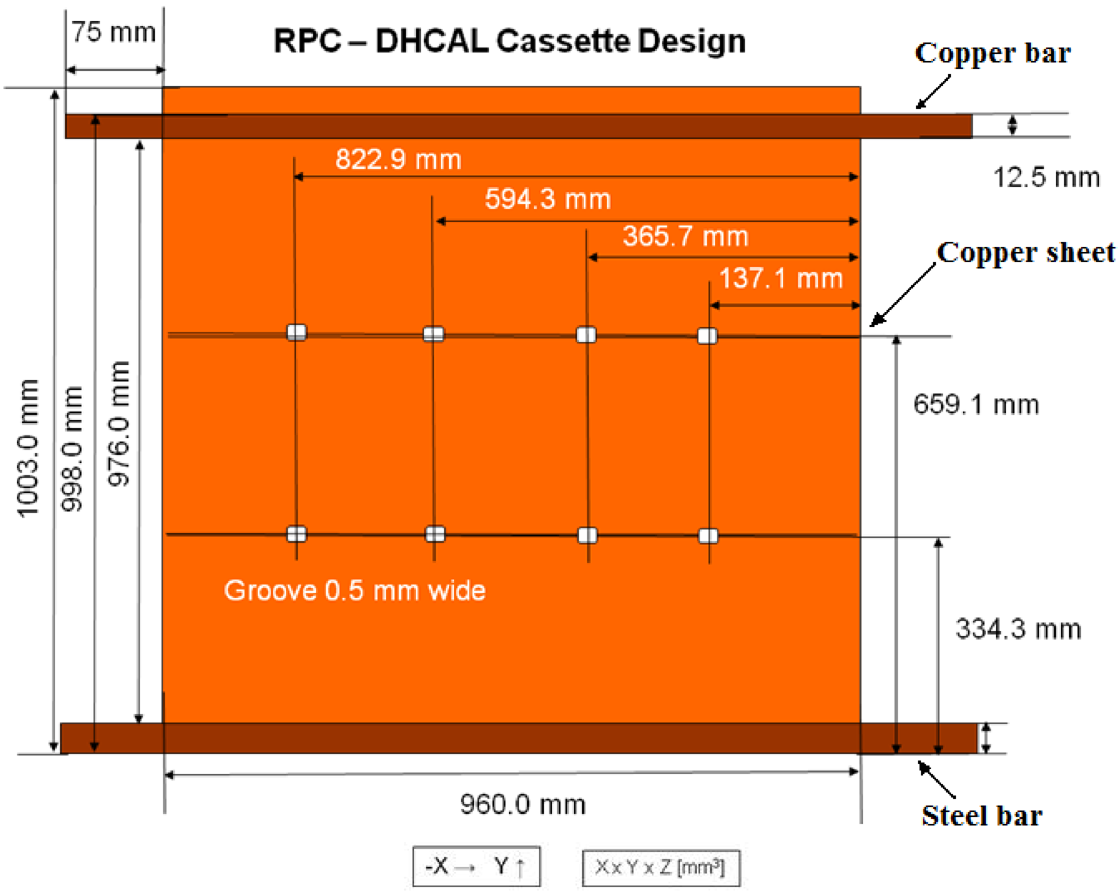

Figure 6.9: Schematic of the DHCAL cassette design without RPCs in it.

Three RPCs were placed between the two bars and six FEBs were placed on the RPCs. Spacers were placed between the FEBs to hold them in place and compensate for the space the RPC frames account for. The space between the top FEB's and the copper bar was 2.7 mm, the space between the top and middle FEBs was 5.2 mm, the space between the middle and bottom FEBs was 5.2 mm and the space between the bottom FEBs and the bottom steel bar was 2.7 mm (see Figure 6.10). The copper sheet was then placed on top of the FEBs and screwed to the top and bottom bars. The badminton strings were then tensioned to approximately 20 lbs and tied off. The excess string was cut so that the knots lied flush to the surface of the copper. There were two additional steel bars placed on the sides of the cassettes going from the top copper bar to the bottom steel bar. These bars were used to ground the system and aided with transportation.

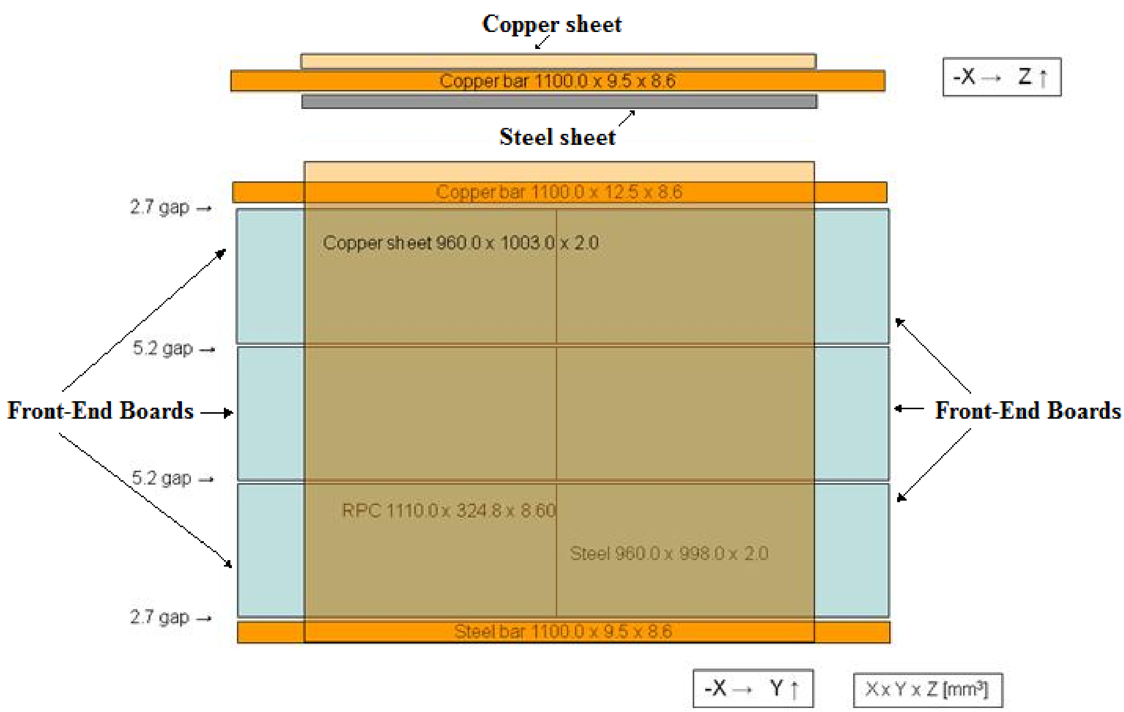

Figure 6.10: Assembled DHCAL cassette schematic illustrating the FEB placement (in blue) as well as the spacing between them.

6.5 Gas system

The gas that goes through the RPCs was a mixture of Freon R134a, Isobutane, and SF_6 (in their respective proportions 94.5 :5.0 :0.5), which gave a large avalanche signal and quick replenish time. These separate gases needed to be mixed on site before going into the chambers. The gas mixer was custom made for the DHCAL and was located outside the enclosure at the test beam. The gas was mixed and sent to a gas distribution system which had 28 channels which could each be individually controlled (see Figure 6.11). Typically each channel of the gas system was split in two so that it could supply gas to two layers. The extra channels were for potential expansions.

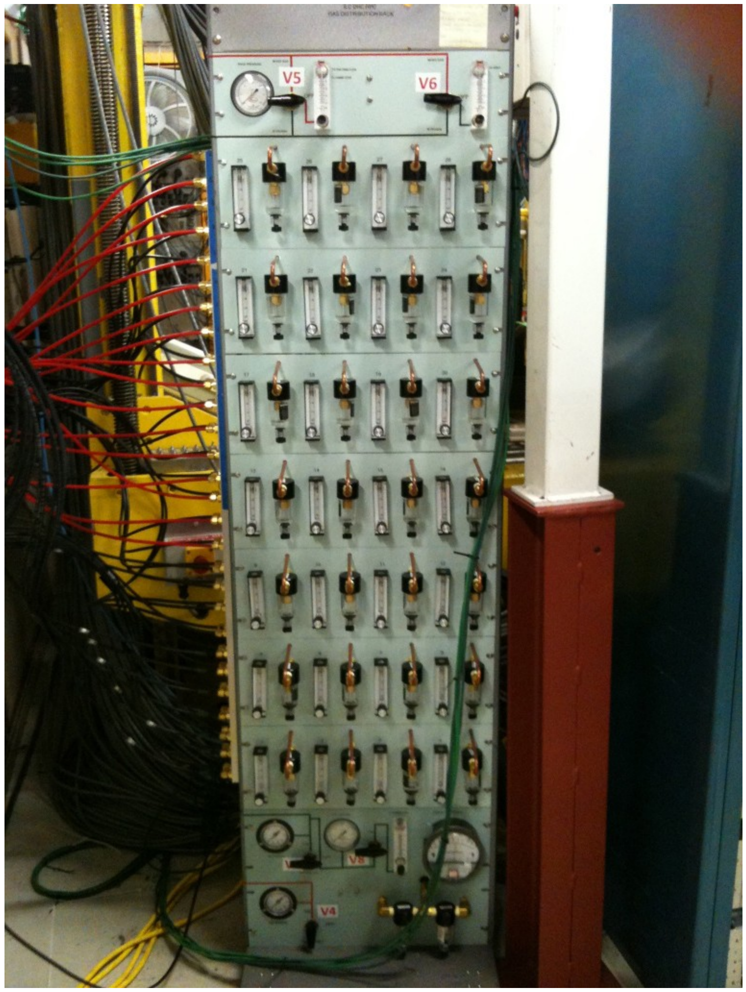

Figure 6.11: Gas distribution system at the Fermi National Accelerator Laboratory test beam area.

Being able to individually control the flow rate of each channel was advantageous when some RPCs were found to have leaks. Increasing the flow rate of some chambers helped to decrease noisy regions by increasing the efficiency and decreasing the multiplicity. When the RPCs were in a cassette the gas flowed as follows: from the bottom of the bottom RPC, out the top of the bottom RPC, to the top of the middle RPC, down to the bottom of the middle RPC, to the bottom of the top RPC and out the top of the top RPC (see Figure 6.12).

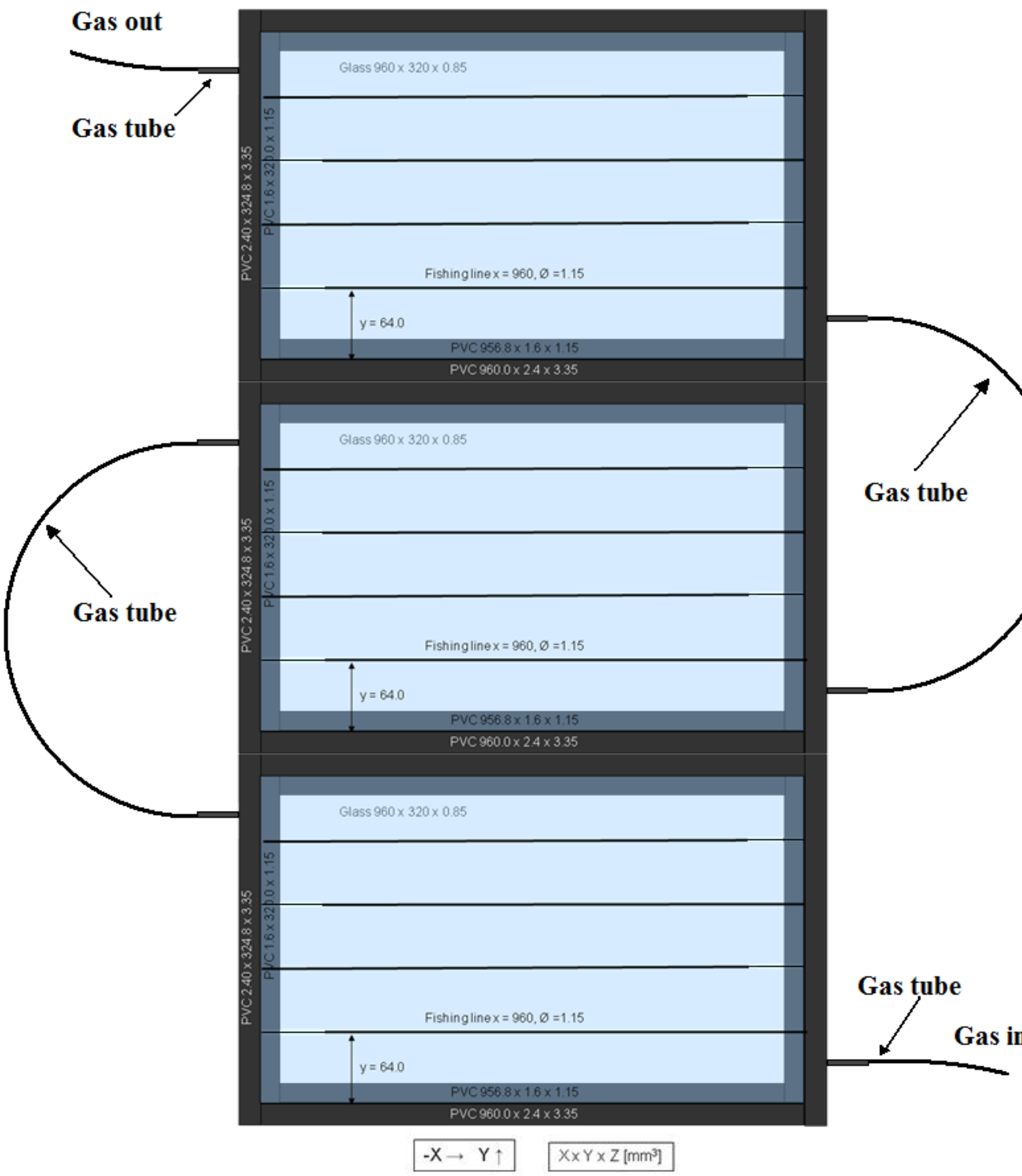

Figure 6.12: Three RPCs stacked vertically on top of each other as in a cassette showing the gas line structure.

6.6 Cosmic ray test stand

The cosmic ray test stand was setup at ANL to test the individual chambers (RPCs were not in cassettes for this), the front-end electronics, and the gas distribution system. This test stand utilized cosmic rays as a source of highly energetic charged particles. The stand consisted of 7 layers initially and then was expanded to 9 layers of RPC modules lying parallel to the ground on plywood sheets separated vertically by 8 cm (see Figure 6.13).

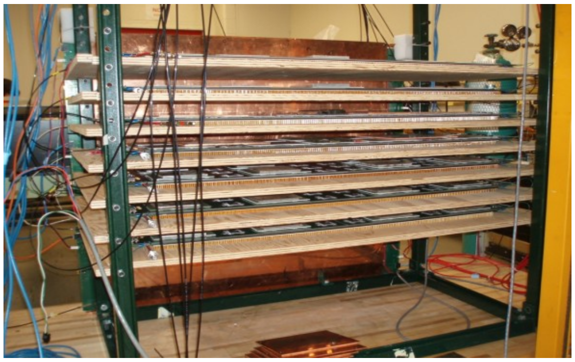

Figure 6.13: Photograph of the cosmic ray test stand when it was equipped with 7 layers of RPCs.

The data samples used for all the analysis of the cosmic ray test stand had approximately 100 000 events combined. They were all combined together to get larger statistics. Each run lasted 5 minutes.

6.7 Fermi Laboratory test beam setup

The test beam was at Fermi National Accelerator Laboratory and took place in October 2010. Figure 6.14 shows a bird's-eye view of the setup. Looking down the beam line the low voltage power supplies along with the gas distribution system were to the left of the DHCAL. The high voltage power supplies and data acquisition VME crates were on the right hand side of the DHCAL. The gas mixer was located in a shed outside of the test beam hall and the TCMT was located directly behind the DHCAL with a separation of 36 cm.

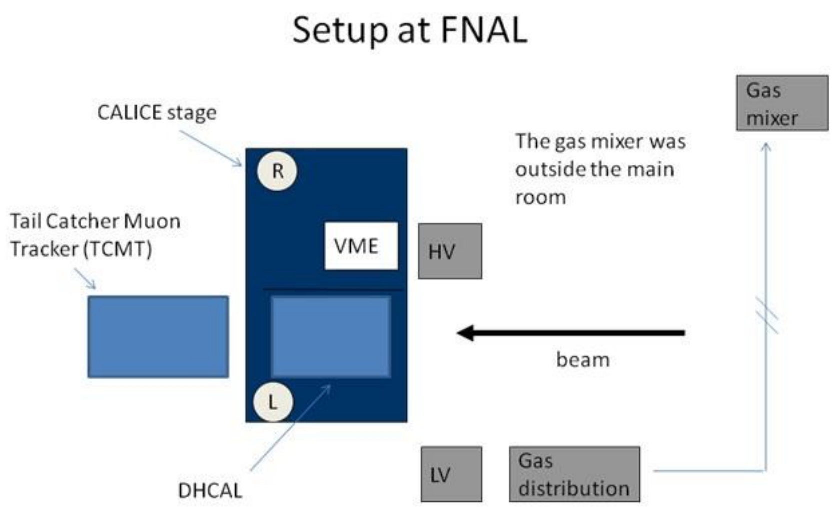

Figure 6.14: DHCAL setup at the Fermi National Accelerator complex test beam area.

The DHCAL was a sampling calorimeter consisting of 38 layers of RPCs and 38 layers of 1.7 cm thick steel absorbers. Each layer of active or passive material excluding the read-out electronics had a surface area of 1 x 1 m^2. An active layer consisted of three 32 cm x 96 cm x 3.15 mm RPCs stacked on top of each other and were put into a cassette as previously seen in Figure 6.10.

The data for this analysis was collected with broadband muons tuned to 32 GeV/c traversing a 3 m thick iron beam blocker. The data acquisition rates were roughly 500 events/spill and the spills were approximately 3.5 s long and came once in a 60 s period. The run number of the data used for the analysis of the DHCAL at the test beam was 610055 and had approximately 65000 events.

6.7.1 High voltage power system

The high voltage (HV) system was used to put a potential difference between the gas gaps in the RPCs. The HV system was made up of three “LeCroy HV4032A” power supplies. The nominal operating voltage of the RPCs was 6300 V (see section 7.2.3). Each channel of the HV power supply was split into three separate lines to power three RPCs. The HV was distributed with RG59 coaxial cables with standard BNC connectors.

6.7.2 Low Voltage Power System

The low voltage (LV) system referred to the power required for the FEBs. The LV system was made up of 5 “Wiener PL508” chassis each of which had six independent 5 V at 30 A subunits power supplies and custom distribution modules made at ANL. One subunit can be seen in Figure 6.15. Each FEB operates with 3 A at 5 V. There were 5 distribution boxes required to fully equip the DHCAL; the boxes were custom made for this project. The distribution boxes corresponded one-to-one with the power supplies and were responsible for sending power to up to 48 FEBs.

Figure 6.15: Low voltage *Wiener* power supply (top) and low voltage power supply distribution box (bottom).

6.7.3 Data Acquisition System

The data acquisition system, or DAQ for short, took the output/signal from the RPCs and sent it to the computer for further analysis. The front-end channel consisted of an amplifier/shaper/discriminator with a 1-bit dynamic range which had a common threshold for all 64 channels per ASIC. The ASICs had a 100 ns time resolution. Each hit got a timestamp which was synchronized over the entire system. The data from a FEB consisted of a hit pattern, timestamps and possible errors. The time was in ns, the hit pattern was given in terms of pad locations and errors could take various forms depending on their type. Possible errors might have occurred if the FEBs were not synced properly, a given ASIC was not responsive, or certain channels were not responsive. The system was able to be self-triggered, i.e. on noise, and cosmic rays. The system was additionally capable of performing external triggering (scintillator paddles, Cherenkov counters) with a 20 data stage pipeline which gave a 2 μs latency to ensure no data was lost while the decision was made whether or not to keep the data. The system was designed for rates up to 100 Hz in external and self-triggering mode.

Each FEB had a data cable that went to a data collector which could accept 12 inputs. The data collectors were connected to the Trigger-Timing Modules (TTM) which were all housed in VME crates (see Figure 6.16). The data collectors were a custom made piece which accepted our data cables. There were two VME crates, one to collect the data from the FEBs on the left half of the DHCAL and one to collect the data from the FEBs on the right half of the DHCAL. One of the VME crates housed two TTMs, one master and one slave, while the second housed just one slave TTM. The extra TTMs set in slave mode were there so that we had enough input channels. The master TTM unit accepted an external trigger from two 1 m^2 sized scintillator paddles which were run through a coincidence unit. The master TTM made the final decision whether or not to send the data to the PC to be recorded. The master TTM sent a signal to a controller on the VME crate to send the data from the FEBs to the computer. This data flow can be seen in Figure 6.16.

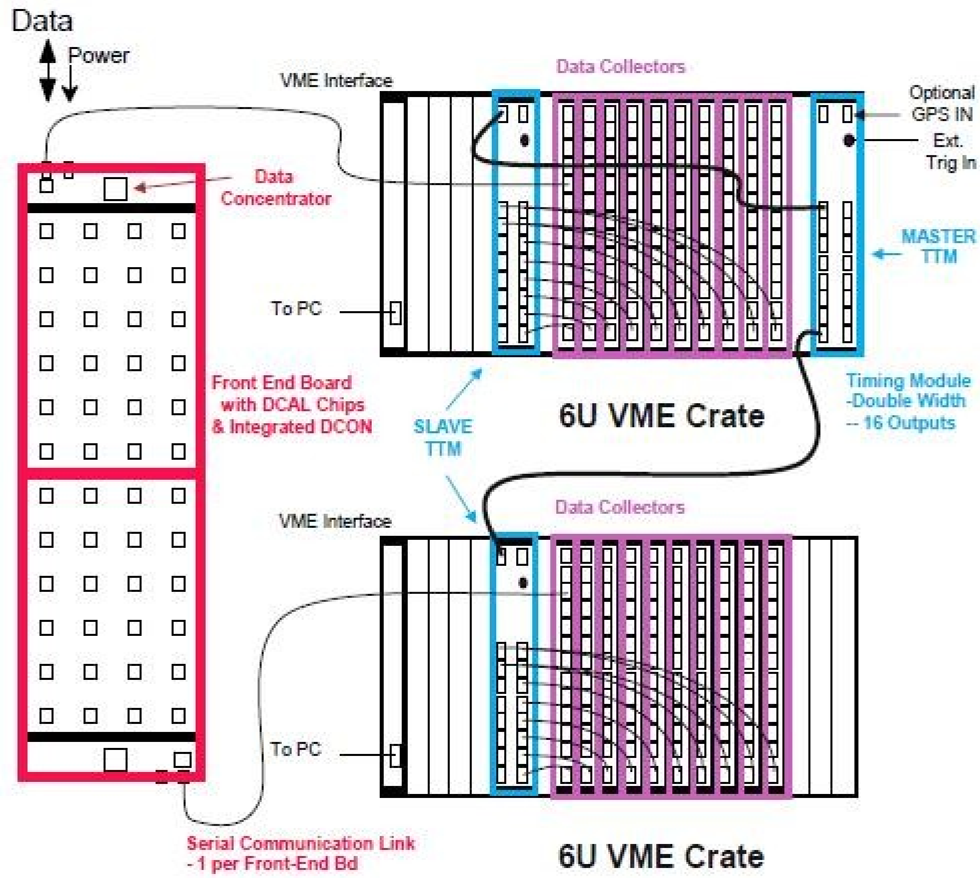

Figure 6.16: DAQ system schematics showing the data flow from the FEB (on the left) to the data collectors in the VME crates (right).

7 Digital Hadron Calorimeter Data Analysis

The DHCAL has taken test beam data with several types of particle beams; Figure 7.1 shows the various particle interactions. There were two modes of running, muon mode as described in section 6.6, and additionally proton mode. The proton mode test beam setup is not described since it will not be used for any of the analysis. The interactions in Figure 7.1 show how the various particles species deposit energy when they impinge on the DHCAL as described in chapter 4.

Muons were chosen for the initial analysis due to their simple interactions. Since the muons will leave straight tracks in the DHCAL, muon events can be reconstructed to check the alignment and response of the RPCs. To calculate the efficiencies of each of the pads on the FEBs we can start by assuming that the muons will leave straight tracks and inter/extrapolate a fit to the data points to determine where the DHCAL should have recorded hits. Ideally we want one pad to fire in a layer when one particle traverses it. The average number of pads that record a signal for a track is the multiplicity. Other particle species cannot be used to calculate such properties since they will start to shower. These particles can be used if only the minimum ionizing particle (mip) track is used and not the hits in the shower. For instance, if a positron enters with high enough energy for it to start an electromagnetic shower then more than one particle may pass through a given pad due to the dense nature of electromagnetic showers. This will skew the value calculated for the pad multiplicity. This is an entirely different problem that will not be discussed any further since it is beyond the scope of this analysis.

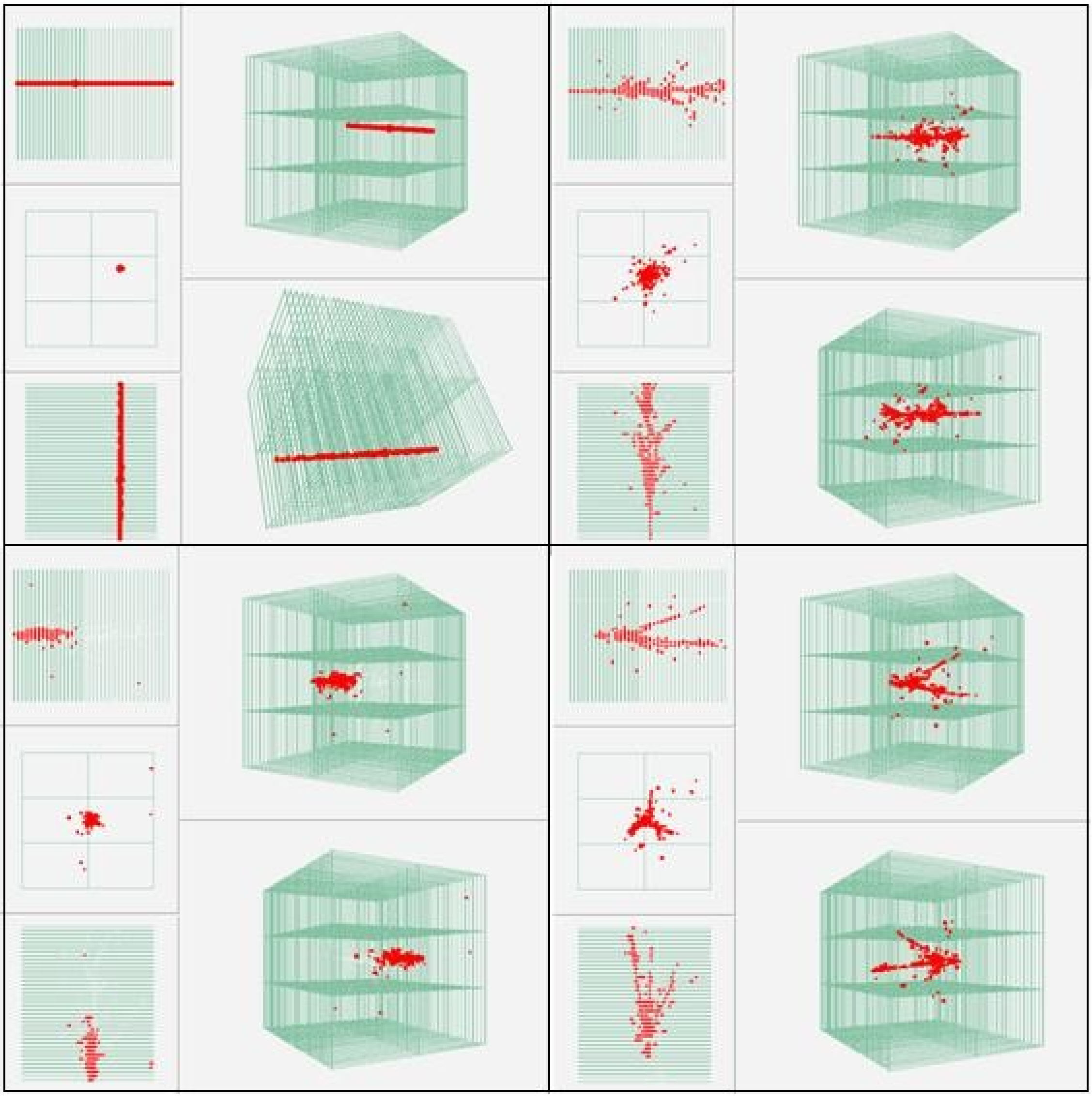

Figure 7.1: Event display of data taken of 4 particle types, top left is a muon event, top right is a pion event, bottom left is a positron event, and the bottom right is a neutral hadron event. Each event display can be broken down into three projected views YZ plane (top left), XY plane (middle left), XZ plane (bottom left) and two isometric views (right).

7.1 Analysis strategy

A cosmic ray test stand was setup at ANL to test the individual chambers, the front-end electronics, and the gas distribution system (section 6.5). The cosmic ray test stand is used to get practice running such a system and to work on the HV connection and test the electronics software, as well as to develop analysis tools for the DHCAL.

The input data is in a tuple (ordered list of elements) format, “timestamp x y z” example: 9585846 10 32 14. The timestamp (in units of 100 ns) is assigned by the Trigger and Timing Module (TTM), the variable x in the tuple is the pad number in the x dimension of the pad that fired, the y variable is the pad number in the y dimension of the pad that fired and the z variable is the layer number of the pad that fired. When the x, y, and z are -1’s this indicates the beginning of a new event. Each line of the data files contains information for one “pad hit” (pad firing) in an RPC. The events may contain zero pads hit up to all the pads being hit. The events are generated by a program called the event builder, and takes data output by the DAQ in a binary format set by the CALICE DAQ binary structure. The events are looked at one at a time and are checked to see if clusters of pad hits can be made. Our definition of a cluster is if two pad hits in the same layer share a common side. Then they are part of the same cluster (clusters can have more than 2 pad hits). In Figure 7.2 (left) the two pads that fired (indicated by the colour red) share a common side and are considered to be part of the same cluster, where as in Figure 7.2 (right) the two pads that fired are not part of the same cluster.

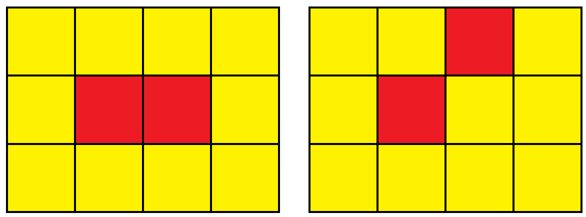

Figure 7.2: Left: two pads which have fired (shown in red) that are part of the same cluster. Right: two pads have fired but are not in the same cluster since they do not share a common side.

Once the clusters are made the average position of the cluster is calculated. The clusters are then filtered by looking only at the layers that have 1 cluster in them. When dealing with a square meter cassette the spacing between the pads in physical space is taken into account by adding a fixed value to the y dimension. The space between the boards is 0.52 cm. The data points are then fitted using a 2D regression method for the (X, Z) coordinates and second 2D fit for the (Y, Z). The points used for track reconstruction are points which are in a layer with only one cluster in them. This avoids reconstructing a track using noise hits.

$$X = a + bZ$$

$$Y = c + dZ$$

Where ‘a’, ‘b’, ‘c’, ‘d’ are the parameters of the straight line.

$$a = \frac{1}{\Delta}\left(\sum_{i=1}^{k} \frac{z_i^2}{\sigma_i^2} \sum_{i=1}^{k} \frac{x_i}{\sigma_i^2} - \sum_{i=1}^{k} \frac{z_i}{\sigma_i^2} \sum_{i=1}^{k} \frac{z_i x_i}{\sigma_i^2} \right)$$

$$b = \frac{1}{\Delta}\left(\sum_{i=1}^{k} \frac{z_i x_i}{\sigma_i^2} \sum_{i=1}^{k} \frac{1}{\sigma_i^2} - \sum_{i=1}^{k} \frac{z_i}{\sigma_i^2} \sum_{i=1}^{k} \frac{x_i}{\sigma_i^2} \right)$$

$$\Delta = \sum_{i=1}^{k} \frac{1}{\sigma_i^2} \sum_{i=1}^{k} \frac{z_i^2}{\sigma_i^2} - \left(\sum_{i=1}^{k} \frac{z_i}{\sigma_i^2} \right)^2$$

$$\sigma_i = \frac{n_i}{\sqrt{6}}$$

where ‘n’ is the number of pads in the given cluster and ‘i’ refers to the i’th cluster point and ‘k’ is the number of clusters. The coefficients ‘c’ and ‘d’ are found analogously by replacing the x’s in the above equations with y’s. The uncertainty in the coefficients are calculated using the following

$$\sigma_a^2 \cong \frac{1}{\Delta} \sum_{i=1}^{k} \frac{z_i^2}{\sigma_i^2} \qquad \sigma_b^2 \cong \frac{1}{\Delta} \sum_{i=1}^{k} \frac{1}{\sigma_i^2}$$

The reduced chi-squared is calculated for each recreated track and is calculated using the following equations

$$\chi^2 = \sum_{i=1}^{k} \left(\frac{\Delta r}{\sigma_i^2 (2N_{TR} - 4)} \right)$$

$$\Delta r = \sqrt{\Delta x^2 + \Delta y^2}$$

where ‘N_{TR}’ is the number of clusters used to reconstruct the track, and Δr (the residual) is the distance between the reconstructed track and the position of the closest cluster in the given layer. The angle of incidence with the front of the detector is then calculated for each reconstructed track. To determine how well the chambers are working certain parameters are looked at for each reconstructed track to determine whether or not it is a false track. The number of clusters in the track (N_{TR}), the reduced chi squared (χ^2), and the residual (Δr) are used to cut out tracks which may not be from a charged particle. The reduced chi squared is not the typical version used in statistics. To ensure clean tracks we require $\chi^2 \leq 1$ and $\Delta r \leq 2.5$ cm, which will be explained more in section 7.3.1. The constraint on N_{TR} varies depending on the data in question. For example, if there are only 6 layers in the cosmic ray test stand then requiring $N_{TR} \geq 6$ does not make any sense, where as if there are 9 layers in the test stand then $N_{TR} \geq 6$ is a reasonable requirement to ensure we look only at “true” cosmic ray events. The chosen criteria for ‘N_{TR}’ will be discussed further in section 7.3.1. This also helps exclude some of the soft muons which stop part way through the test stand and so do not traverse in the later layers of the detector. The cuts on the data will be validated in the section 7.3.1. The data leftover after the cuts are then used to calculate the efficiency and multiplicity of each of the RPCs. The efficiency, multiplicity and corresponding errors are calculated for any area. This could be an average over the entire chamber, for each pad, for each chamber, or some other area larger than a pad. Typically the efficiencies and multiplicities are calculated for each layer, all layers, and for each pad. These quantities are calculated for the different areas to get an idea of the overall response, and a more detailed response for certain areas which may be problematic. The efficiency for an area is defined as follows

$$\varepsilon = \frac{N_{cf}}{N_{csf}}$$

where 'N_{cf}' is the number of times a hit is recorded when a particle traversed that area within a distance of 'Δr' to the reconstructed track, and 'N_{csf}' is the number of particles that traversed the area (both recorded and not recorded). These numbers are determined by examining the tuple file, looking through each event and counting the number of times $\Delta r \leq 2.5$ and dividing by the number of tracks that should have and did go through the area. If there is not a cluster there the efficiency is reduced.

The pad multiplicity is a measure of how many pads give a signal when a particle is incident on the chamber. The multiplicity is a measure which is chamber-dependent and thus does not count the total number of pads that fired in the whole detector for one track. Instead it counts the number of pads in a cluster and averages over all the events in the given region. In equation form it can be written as the following

$$\mu = \sum_{i}^{k} \frac{Ncl_i}{k}$$

Where 'k' is the number of clusters, 'Ncl' is the number of pads in a cluster, and the zero's are not counted. The efficiency is a binomial distribution and thus the error in the efficiency was calculated using the following

$$d\varepsilon = \sqrt{\frac{\varepsilon(1-\varepsilon)}{n}}$$

where 'n' is the total number of events and 'ε' is a percentage(less than 1). The error in 'µ' is calculated with

$$dNcl = \sum_{i}^{k} \sqrt{\frac{(Ncl_i - Ncl_{avg})^2}{k}}$$

where 'k' is the number of clusters for the given region for which 'Ncl' is calculated. Data falling in the region 0.5 cm around the edge of a chamber are removed to ensure that no tracks went outside the detector. The dead space accounts for ~4% of the area of a cassette.

The average efficiency and its uncertainty of the entire detector is calculated with the following formulae

$$\langle\varepsilon\rangle = \frac{\sum_i^n \left(\varepsilon_i / \sigma_i^2 \right)}{\sum_i^n \left(1 / \sigma_i^2 \right)} \qquad \sigma_\varepsilon^2 = \frac{1}{\sum_i^n \left(1 / \sigma_i^2 \right)}$$

where ‘n’ is the number of layers and ‘σ^2_i‘ are the errors for the individual layers.

The multiplicity and its uncertainty are calculated with the following formulae

$$\langle\mu\rangle = \frac{\sum_i^n \left(\mu_i / \sigma_i^2 \right)}{\sum_i^n \left(1 / \sigma_i^2 \right)} \qquad \sigma_\mu^2 = \frac{1}{\sum_i^n \left(1 / \sigma_i^2 \right)}$$

where ‘n’ is the number of layers and ‘σ^2_i‘ are the errors for the individual layers.

7.2 Cosmic ray test stand results

This section covers the analysis results of the cosmic ray test stand data. The analysis will contain a study of the efficiencies and multiplicities of the chambers, the performance of the chambers with changing angle of incidence of the incident particles and the effect of the operating voltage on its overall performance. Recall that the cosmic ray test stand only has one RPC per layer as described in section 6.5.

7.2.1 Efficiencies and Multiplicities

The efficiencies of the RPCs in the test stand are calculated for each 8 cm by 8 cm area due to the low statistics. A sample is shown in Figure 7.3 of the efficiencies of layers 0 and 1. The x and y axis correspond to the position of the square areas and the colour designates the value of the efficiency for that area.

Efficiencies in layers 0 and 1 binned in 8cm x 8cm areas

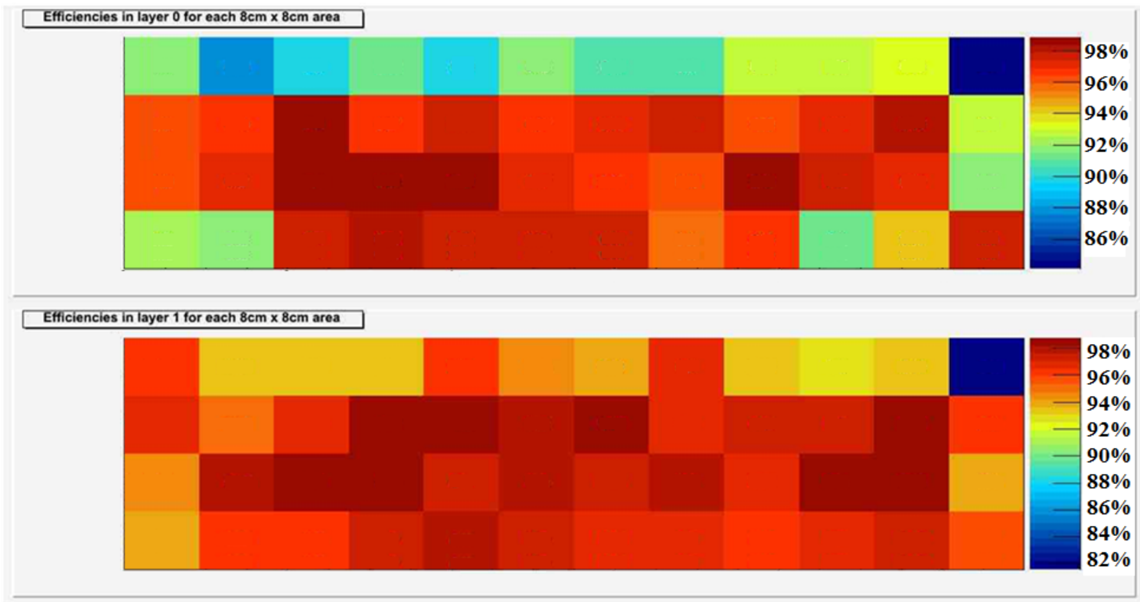

Figure 7.3: Efficiencies of top two layers split into 8 x 8 cm^2 areas.

The top edge of layer 0 is less efficient than the rest of the chamber; this could be caused by several things such as: a misaligned RPC, poor connectivity of the FEB to the pad board, or a larger gas gap. Overall the efficiencies are acceptable and mostly in the mid 90% range with the exception of the top right corners. The top right corners likely have an increased gap size which decreases the efficiency (see below). Each data taking run period lasted 5 minutes.

The multiplicities of each RPC in the test stand are calculated for the same 8 cm by 8 cm areas as the efficiencies. Figure 7.4 is a plot of the multiplicities of layers 0 and 1. The x and y axis correspond to the position of the square areas and the colour designates the value of the multiplicity for that area.

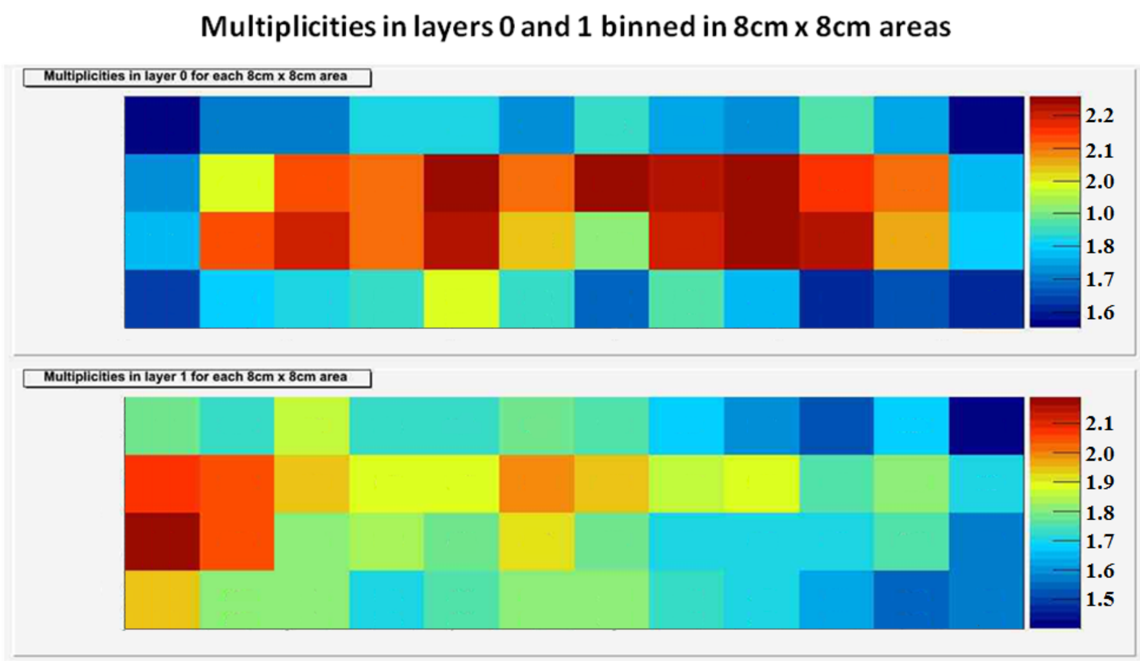

Figure 7.4: Multiplicities of the top two layers split into 8 x 8 cm^2 areas.

The multiplicity in layer 0 is significantly higher in the middle of the chamber than the edges. The multiplicity in layer 1 is higher on the far left side of the RPC, this is likely due to the high voltage connection at that point which tends to be a hot spot. Ideally the high voltage connection would create a uniform electric field however this is not always the case in practice and the increased field strength at this location will increase the multiplicity. The correlations between the efficiencies and multiplicities will be shown in Figure 7.10.

The use of cosmic rays is very important to understand how the RPCs will respond in the test beam since we will use a muon beam initially to calibrate the DHCAL. We are able to test each RPC and FEB individually before installing them into the test beam and make repairs if needed. These tests also allow us to determine an optimum operating voltage for the chambers. Additionally we are able to start making analysis tools which can be extrapolated and used for the completed DHCAL prototype in the test beam runs. There are correlation plots of the efficiencies and multiplicities to follow in section 7.2.2.

7.2.2 Angular dependence

The cosmic ray test stand (Figure 6.13) is used to determine the angular dependence on the efficiencies and multiplicities. The angular distribution of the cosmic rays can be seen in Figure 7.5 which is generated by our analysis. The angle is measured from the normal to the surface of the RPCs.

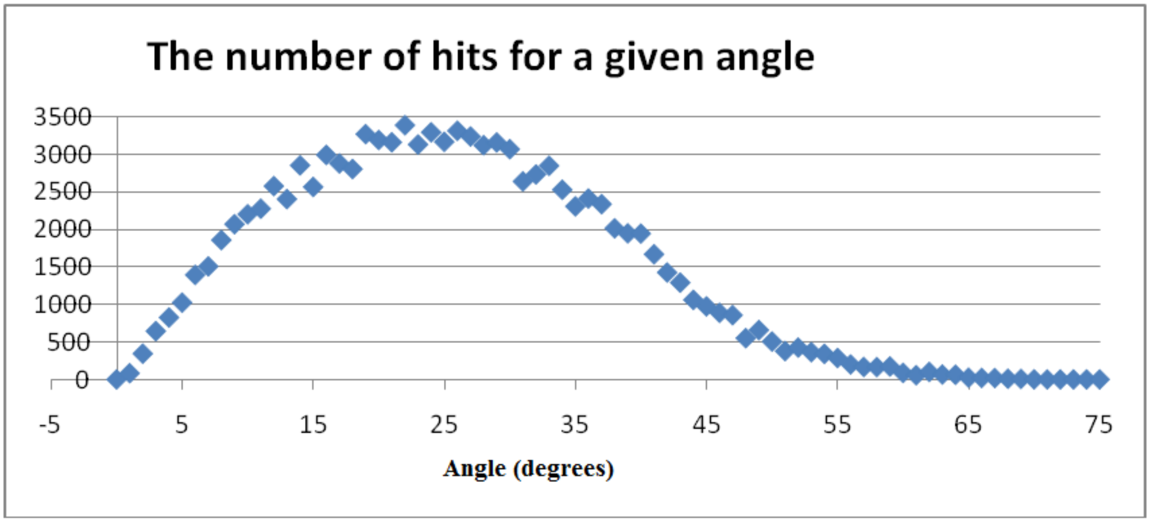

Figure 7.5: Histogram of the number of hits of cosmic muons through a range of incident angles for an entire run.

It is clear from Figure 7.5 that the majority of the cosmic rays do not come perpendicular to the earth's surface. The angle at which the most cosmic rays are incident is 23 degrees from the normal of the surface. This is a geometrical effect since the solid angle will increase as you move away from zero (perpendicular to the detector). Additionally, when one integrates further and further away from the zero degrees zenith the angle of acceptance decreases and therefore one will not see the greatest flux at angles approaching 90°. The combination of the acceptance angle decreasing and acceptance angle increasing will cause this optimum value of 23 degrees.

Demonstrated in Figure 7.6, the efficiency does in fact depend on the angle by roughly 10% through the spectrum.

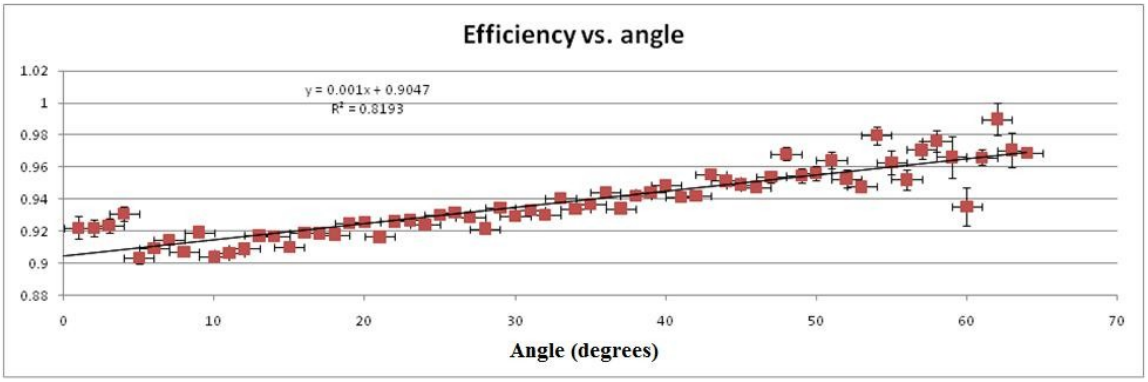

Figure 7.6: Efficiency as a function of angle for cosmic ray muons incident on the cosmic ray test stand.

Similarly the multiplicity as a function of the incident angle is investigated and has shown a clear dependence changing by 0.2 across the spectrum as seen in Figure 7.7. There is currently no explanation for the break in the data at approximately 5 degrees.

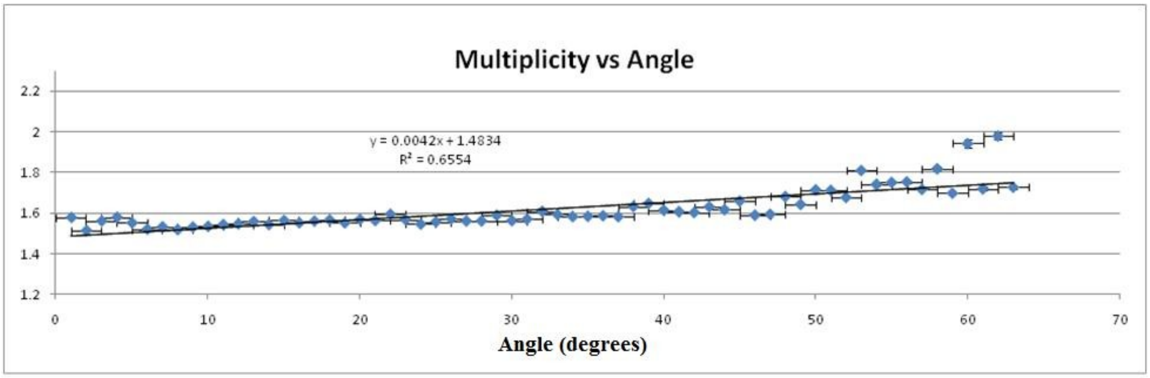

Figure 7.7: Multiplicity as a function of angle for cosmic ray muons incident on the cosmic ray test stand.

The increase in both efficiency and multiplicity is expected since at higher angles the path the charged particle travels through the gas is increased which will in general increase the number of ionizations creating a bigger avalanche. The variation in the multiplicity (~15%) is not enough to cause concern for the system's performance. The multiplicity would have to be much closer to a value of two to warrant a large concern. Additionally, a typical event in the test beam does not have a large angle.

7.2.3 Voltage dependence

The 9 layers in the cosmic ray test stand are used to determine the voltage dependence on the efficiency and multiplicity of each of the modules, in particular the high voltage put across the anode and cathode glasses. Figure 7.8 depicts the strong relation the voltage has on the efficiency of each of the 9 modules.

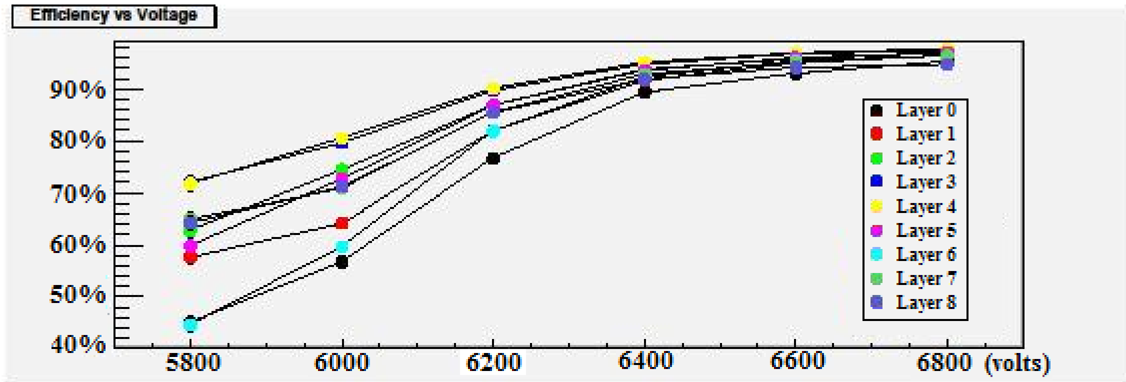

Figure 7.8: The efficiency of each of the 9 layers in the cosmic ray test stand as a function of the operating voltage.

Similarly Figure 7.9 displays the functional dependence of the multiplicity with changing the high voltage.

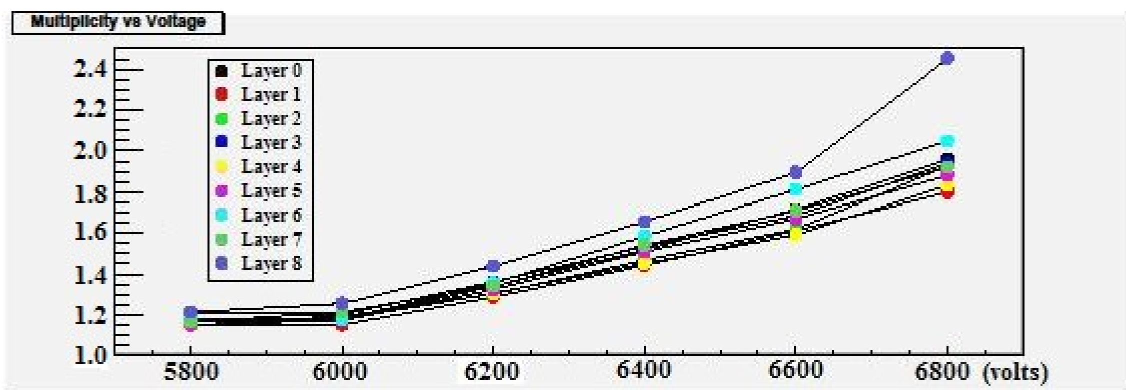

Figure 7.9: The multiplicity of each of the 9 layers of the cosmic ray test stand as a function of the operating voltage.

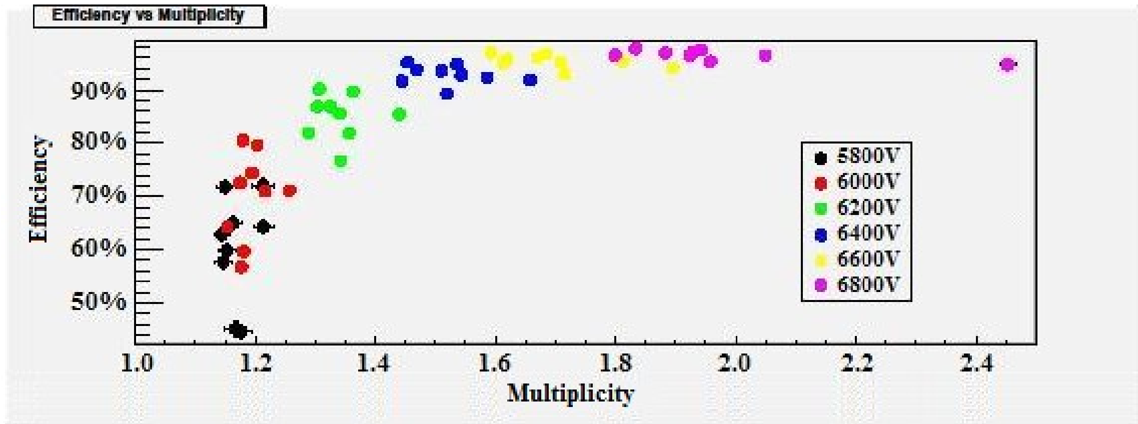

Figure 7.10: The efficiency as a function of the multiplicity for the various operating voltages of the RPCs in the cosmic ray test stand.

Figure 7.10 illustrates the strong relation between the efficiency and multiplicity for various operating voltages, the higher the voltage the higher both the efficiency and multiplicity are, thus a compromise is made to decide what the best operating voltage is. It is decided that the HV should be set to 6.3 kV in order to have an efficiency greater than 90% with multiplicity as close to 1 as possible.

7.3 Fermi test beam facility analysis with muon beam

The muon beam analysis is crucial for the next stages of the analysis. In the following section we study our track fitting algorithms and its effects on quantities such as the efficiencies and multiplicities of the RPCs. The alignment is calculated based on the muon tracks and is therefore important to understand all of its intricacies.

7.3.1 Systematic study

This section discusses the cuts made on the data and explores the decision making of where to place the cuts and how to select the data.

The initial cuts made are:

χ^2 ≤ 1, Δr ≤ 2.5 cm, Ncl ≤ 5, N_{TR} ≥ 15 where 'χ^2 ' and 'Δr' are the same as in section 7.1, 'Ncl' is the number of pads in a cluster, and 'N_{TR}' is the number of clusters in a track. The validity of these cuts is investigated next. To investigate the restrictions on the data all the cuts are removed except the cut on 'N_{TR}' which is a very loose restriction for a muon event since they generally go right through the entire calorimeter and should have a hit in every layer. The reduced chi squared distribution can be seen in Figure 7.11 with all the cuts removed excluding the cut on the number of clusters in a track. The cut on the number of clusters in a track is put at 5 or more. This cut removes noise events.

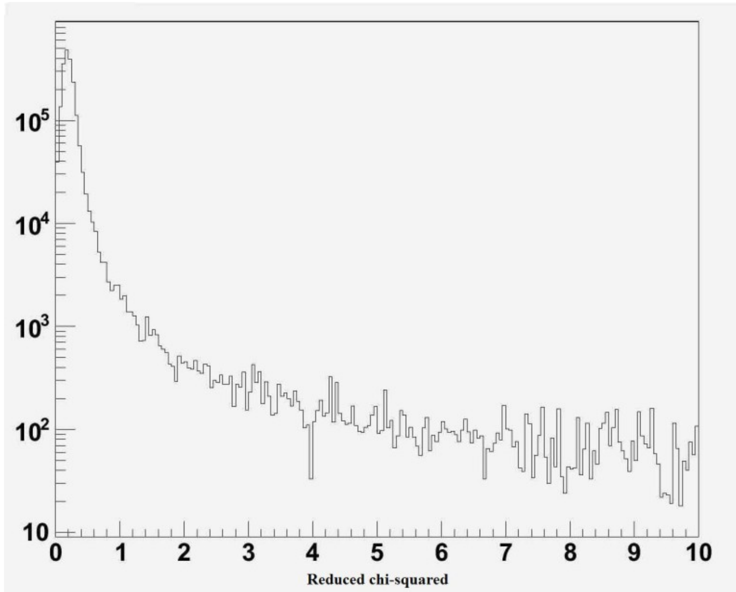

Figure 7.11: A Histogram of the χ^2 values for the track candidates.

Looking at the distribution of the reduced chi squared in Figure 7.11, the cut at 1 has little effect. The data in Figure 7.12 has all cuts removed with the exception of the cut on 'N_{TR}>15'.

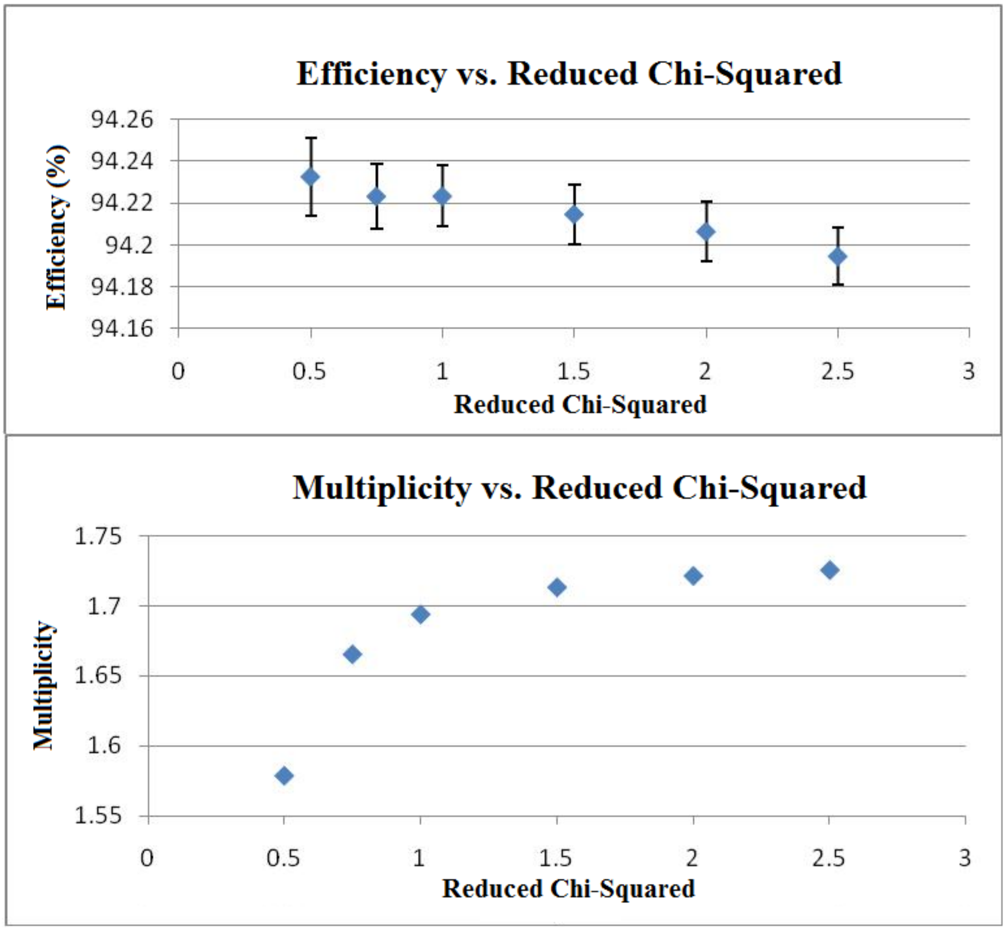

Figure 7.12: The efficiency (top) and multiplicity (bottom) as a function of the 'χ^2'.

It can be seen in Figure 7.12 that the efficiency only varies by 0.04% over the range of 'χ^2'. This means that the efficiency is not affected much by cutting on the 'χ^2'. If we look at the multiplicity as a function of 'χ^2' then it can be seen that the cut on 'χ^2' of less than or equal to one is reasonable since the multiplicity is not too high (2 or above) and it does not cut out too much data.

The data used for Figure 7.13 has all the cuts removed except a cut on the number of clusters in a track. This cut on the number of clusters in a track is at 5 or more. The residual distribution is shown in Figure 7.13 and shows that the residuals are typically less than 1 cm. This indicates that the muons leave predominantly straight tracks.

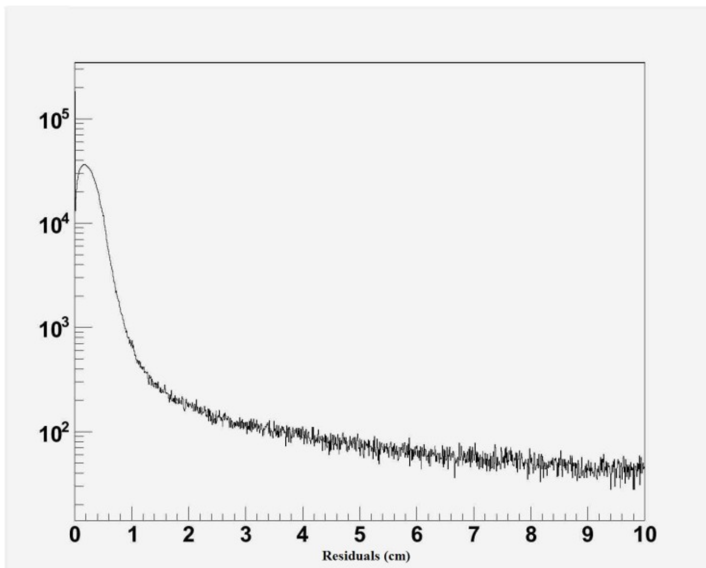

Figure 7.13: The residual distribution for all the tracks with all the cuts in place.

The data used for Figure 7.14 has all the cuts removed except the cut on ‘N_{TR}’ and shows the efficiency and multiplicity as functions of the residuals.

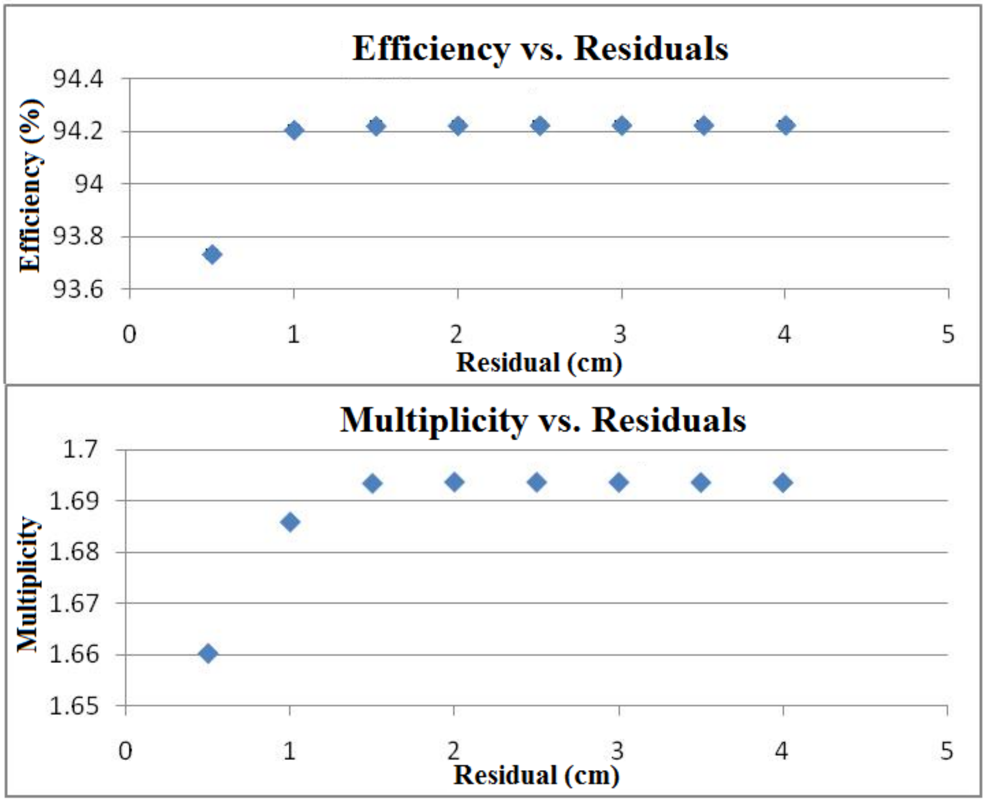

Figure 7.14: The efficiency (top) and multiplicity (bottom) as a function of the residual cut.

From Figure 7.14 the range of the residuals changes the efficiencies by less than 1% and the multiplicities by less than 0.035 which is relatively insignificant. This makes it such that the performance is not dependant on this cut and that the cut at 2.5 cm is acceptable.

We now look at the number of hits per cluster (‘Ncl’) to see if the cut is valid. All the cuts are removed in Figure 7.15 with the exception of the cut on the number of clusters in a track. The cut on the number of clusters in a track put at 5 or more. Figure 7.15 displays the distribution of ‘Ncl’, and it can be seen that the majority of clusters are a single pad. The bin from 0.5-1.5 is contains the ‘Ncl’ equal to one.

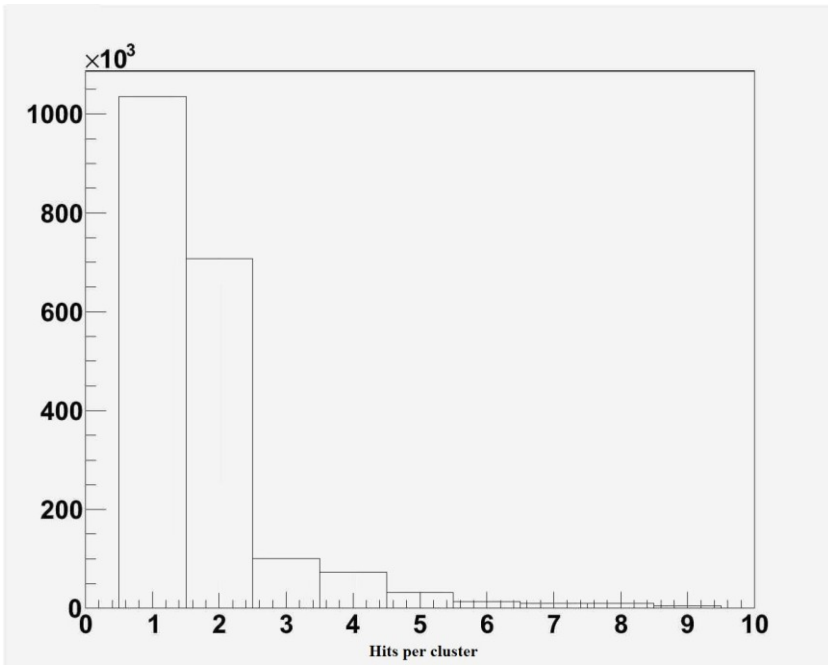

Figure 7.15: The number of pads in a cluster for all the events in a single run.

Figure 7.16 shows the efficiency and multiplicity as a function of ‘Ncl’ with all the cuts removed except the cut on ‘N_{TR}’.

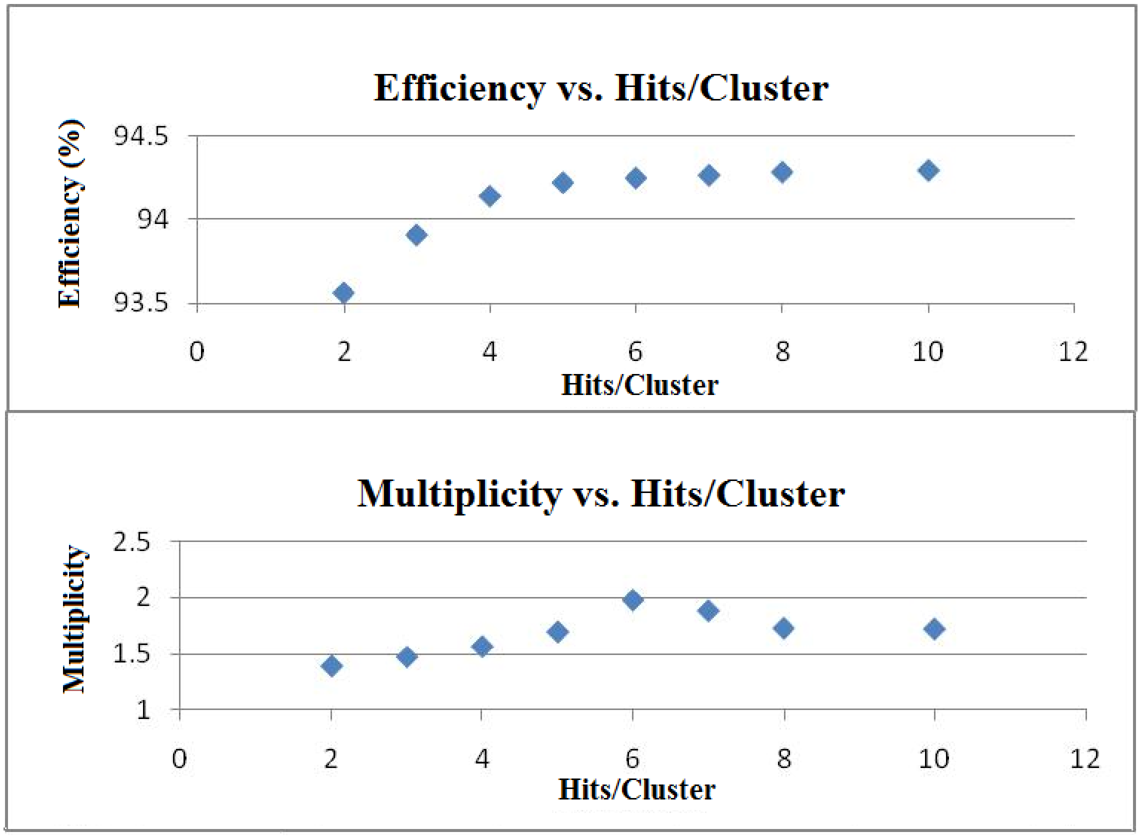

Figure 7.16: The efficiency (top) and multiplicity (bottom) as a function of the number of hits per cluster.

There is only a deviation of less than 1% in efficiency over the 'Ncl' range. The trend in the multiplicity is currently not explainable. Over all it appears that this cut does not do much. The rationale behind this cut was to cut out the events where a FEB had an error and all the pads would register a hit. It is found that these types of events happen only when the temperature of the DHCAL is above approximately 35°C.

Figure 7.17 displays the number of clusters 'N_{TR}' in an event for all the events in a given run with all the cuts removed.

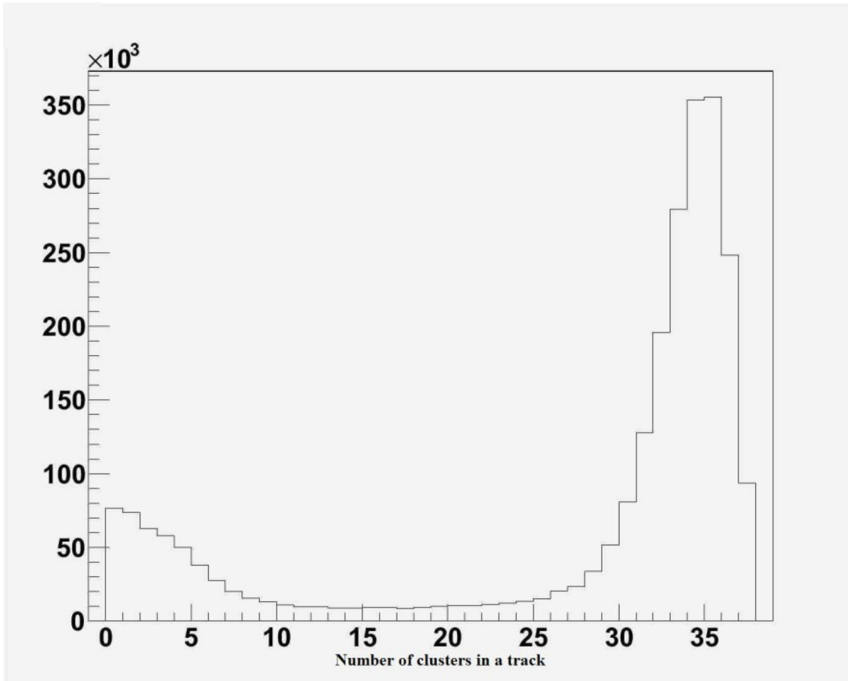

Figure 7.17: Histogram of the number of clusters 'N_{TR}' in a given track for an entire run.

The cut is placed to remove tracks with less than 15 clusters and from the distribution it appears to be an arbitrary choice. The efficiency and multiplicity as functions of the number of clusters in the track gives more insight into where to place the cut. One caveat is that as 'N_{TR}' increases this will artificially increase the efficiency which can be seen in Figure 7.18. The multiplicity as a function of the number of clusters in a track shows that at 15 and higher the multiplicity starts to increase more rapidly. We keep the cut at 15 so that we take some events that still have lower multiplicity but avoid increasing the efficiency (see Figure 7.18).

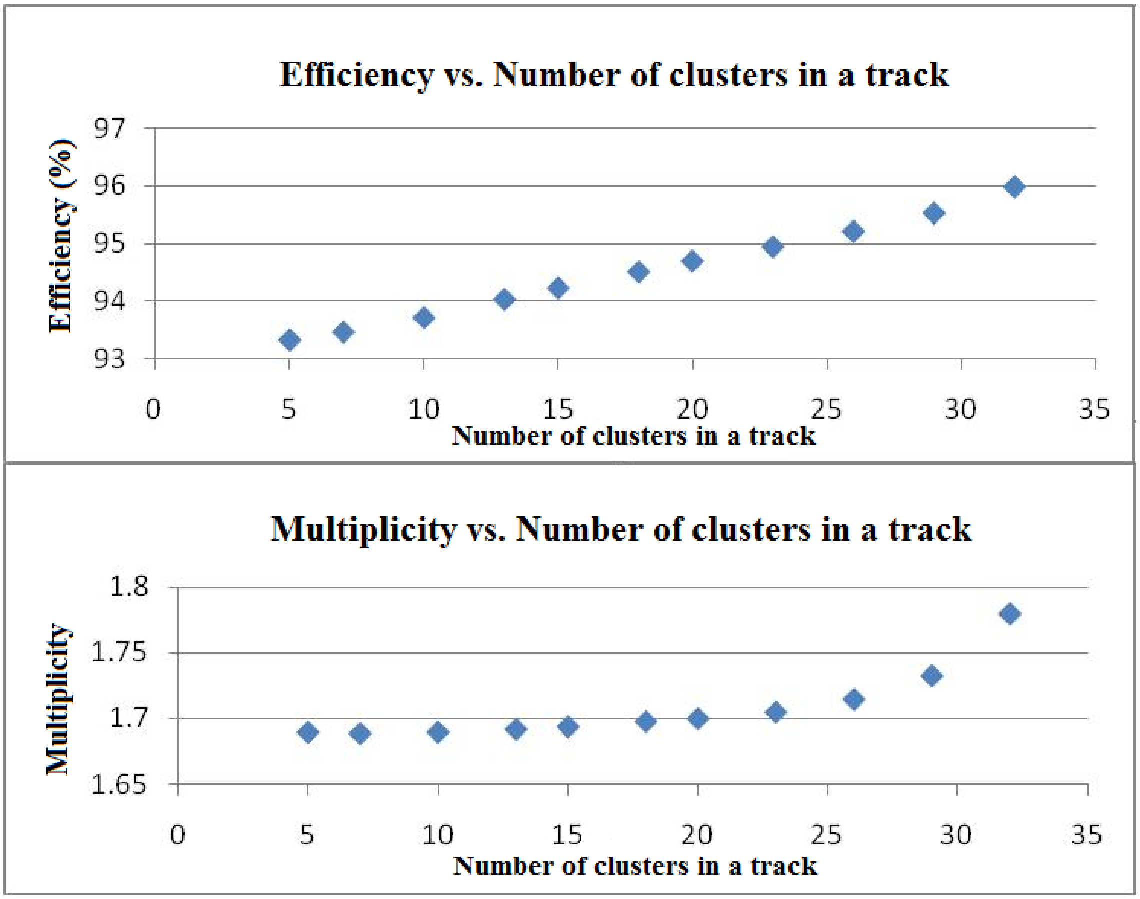

Figure 7.18: The efficiency (top) and multiplicity (bottom) as a function of the number of layers hit.

7.3.2 Efficiencies and multiplicities

The efficiencies of each pad can be mapped out to see poorly working pads or areas which are dead (not firing). A sample of such a view can be seen in Figure

7.19 which illustrates the efficiencies of each pad in layers 18 and 19. Layer 19 is what a typical layer looks like with lower efficiencies at the frames of the RPCs (at y=32 cm and 64 cm and outside edges). The gas barriers also reduce the efficiency and this can be seen every 6.4 cm by a slightly different colour. Layer 18 is shown on the left in Figure 7.19 to illustrate the difference between a good and bad RPC.

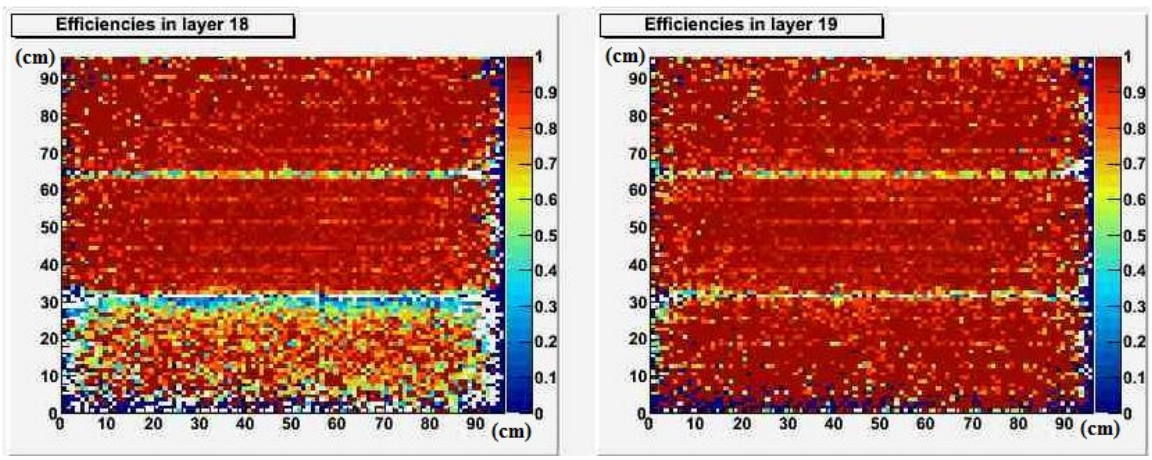

Figure 7.19: The efficiencies of pads in layers 18 (left) and 19 (right) of the DHCAL.

The bottom RPC of layer 18 is very inefficient and has a much different colour than the rest of the layer. These plots are useful tools in determining if something is wrong with a layer or RPC and also potentially useful to determine what the problem is. The bottom RPC in layer 18 is uniformly inefficient and is due to a bad chamber and not a bad FEB. This chamber is to ultimately be replaced and studied to determine why it is behaving in this manner. The associated multiplicities for the layers 18 and 19 can be seen in Figure 7.20.

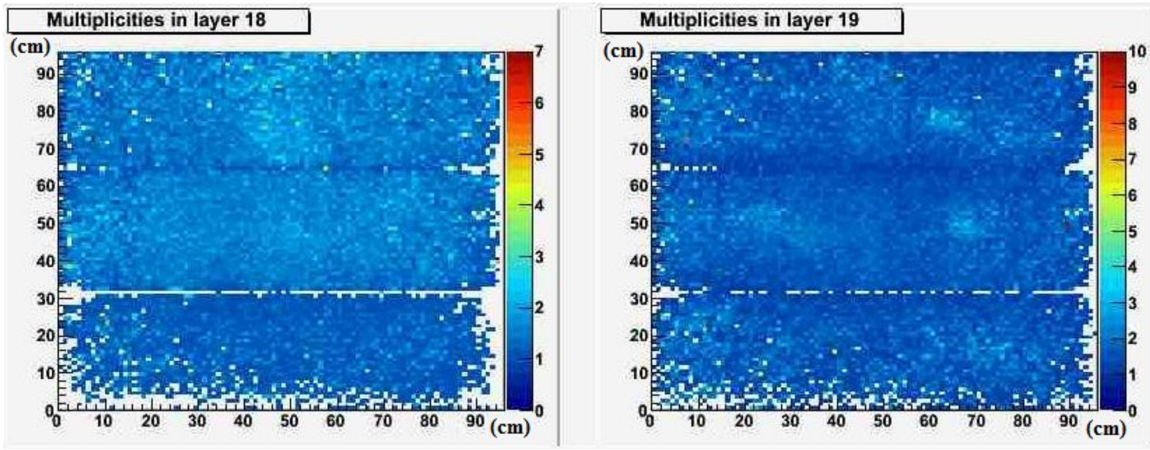

Figure 7.20: The multiplicities of layers 18 and 19 binned into 1 x 1 cm^2 cells.

The bottom RPC in layer 18 is showing a zero multiplicity around the bottom and sides which complement the plot of the efficiencies. The efficiencies of each chamber in the DHCAL are plotted to get a better picture of what is working.

Figure 7.21 shows the efficiencies of each layer in black, the efficiencies of the top RPCs in blue, the efficiencies of the middle RPCs in green, and the efficiencies of the bottom RPCs in red.

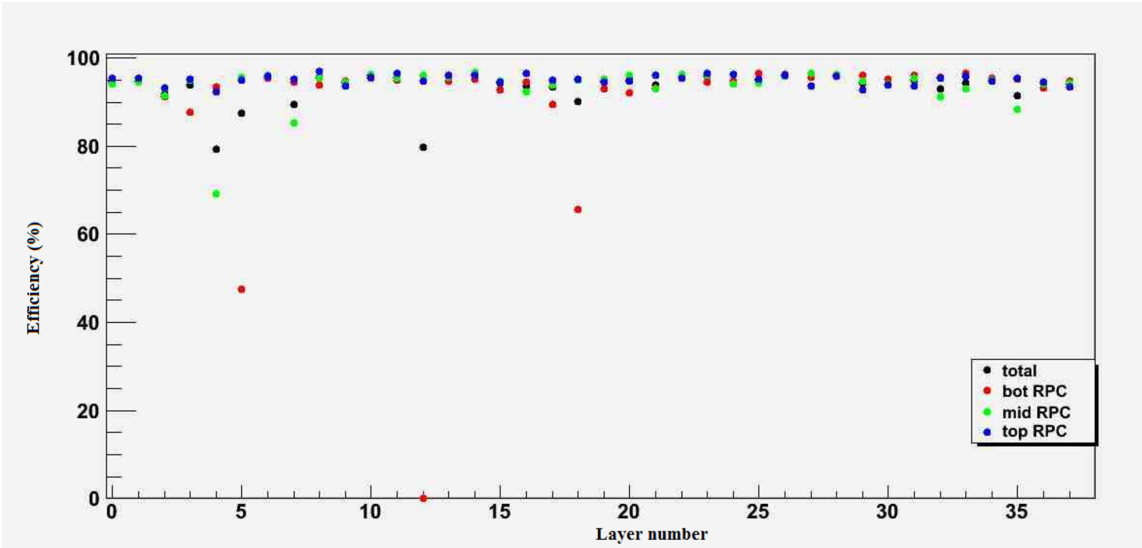

Figure 7.21: The efficiencies for each RPC in each layer and the total efficiency of each layer.

This plot shows that there are four chambers that are less than 80% efficient and that one of them is approximately 0% efficient. The bottom chamber in layer 12, the middle RPC in layer 4, bottom RPC in layer 5, and the bottom RPC in layer 18 are all to be changed out later for better RPCs. The bad RPCs have to be completely investigated and repaired. Figure 7.21 can be used together with plots like those seen in Figure 7.18 to determine why the efficiency of a certain layer/RPC is outside the normal range. For example, the overall efficiency of an RPC could be low due to a few dead ASICs as opposed to an overall low efficiency for the whole chamber. The two plots are complimentary for such an analysis.

Similarly, the multiplicities of each RPC in the DHCAL are plotted in Figure 7.22.

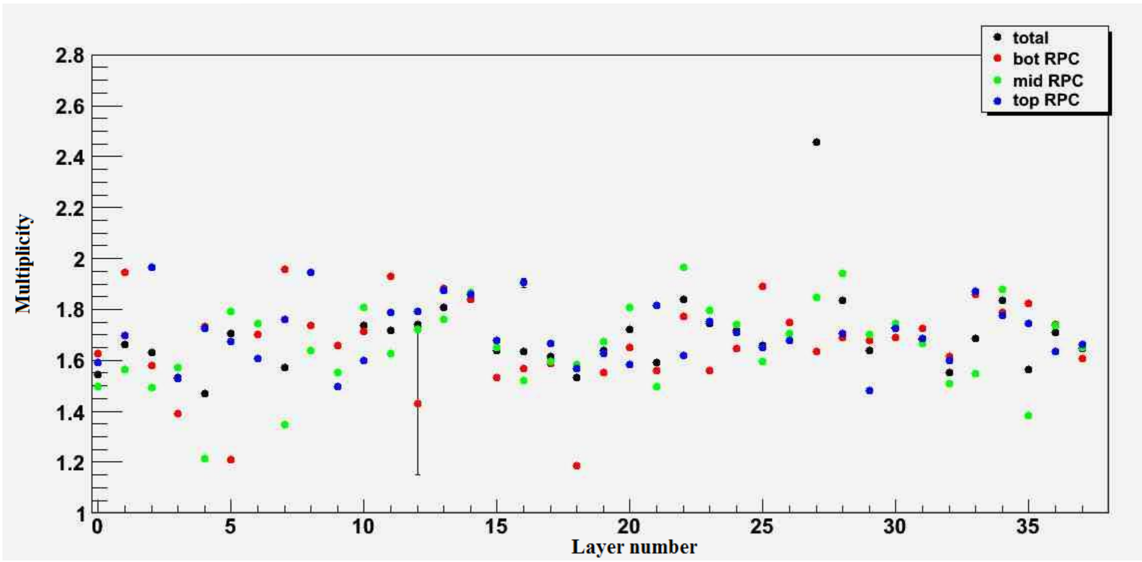

Figure 7.22: The multiplicities for each of the RPCs in all the layers and the total multiplicity for each layer.

From Figure 7.22 the error bars on the multiplicity of the bottom RPC of layer 12 show that there are low statistics. There are low statistics because that chamber is dead. It can also be seen that the top RPC of layer 27 has a multiplicity outside the range of the plot (it was checked to be approximately 4.5) and is very noisy. This can be caused by a gas leak or if the inside of the chamber is not cleaned properly.

Another analysis tool used is a plot of the multiplicity versus the efficiency of each chamber as seen in Figure 7.23.

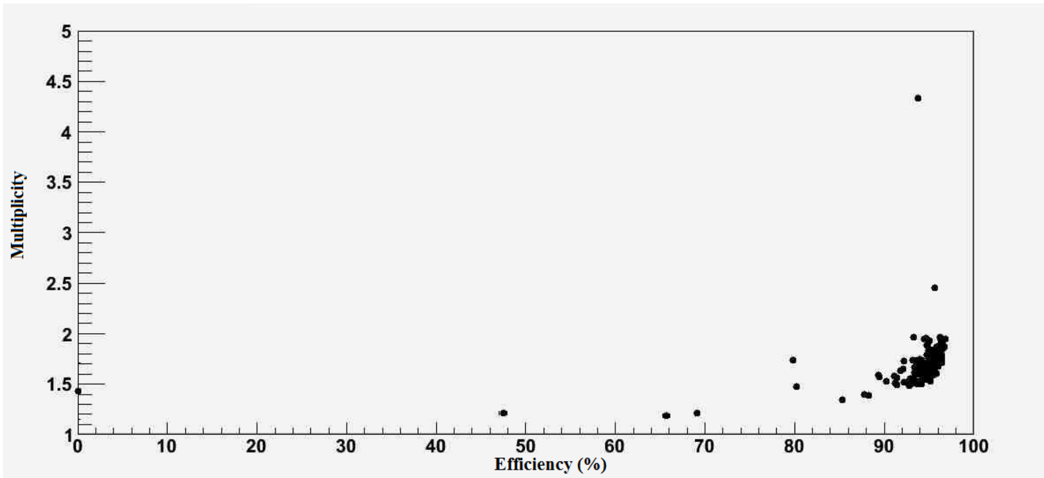

Figure 7.23: The multiplicity versus the efficiency for all the RPCs in the DHCAL.

It is fairly obvious as to which chambers are the outliers in Figure 7.23 since the majority of the chambers are all grouped together. It can be seen that approximately eleven chambers are outside the normal and are worth looking into to determine what the problem is. These chambers have not been checked to date. When the efficiency is just a bit low the HV can be increased to try to compensate, however there are some draw backs. The down side to increasing the HV is that the multiplicity and noise will also increase creating larger uncertainties when analyzing the data.

7.3.3 Impact parameters

To test our understanding of the physics and our detector we should be able to reproduce the same results for the efficiencies/multiplicities with simulations. The DHCAL is simulated with Geant4 [33] (a Monte Carlo based framework used to simulate the passing of particles through matter). In order to have an accurate simulation we also need to have the proper input parameters. The distribution in the x and y directions of the incident beam as well as the angle of incidence need to be properly simulated. A simple analysis of the data sufficed in determining such parameters. The impact parameters of interest are the position and angle at which the beam would enter the calorimeter. The distribution of the position in the x direction is shown in Figure 7.24. The distribution is fitted with a Gaussian and has a mean of 46.3 cm and standard deviation of 22.3 cm. These values are to be put into the simulation.

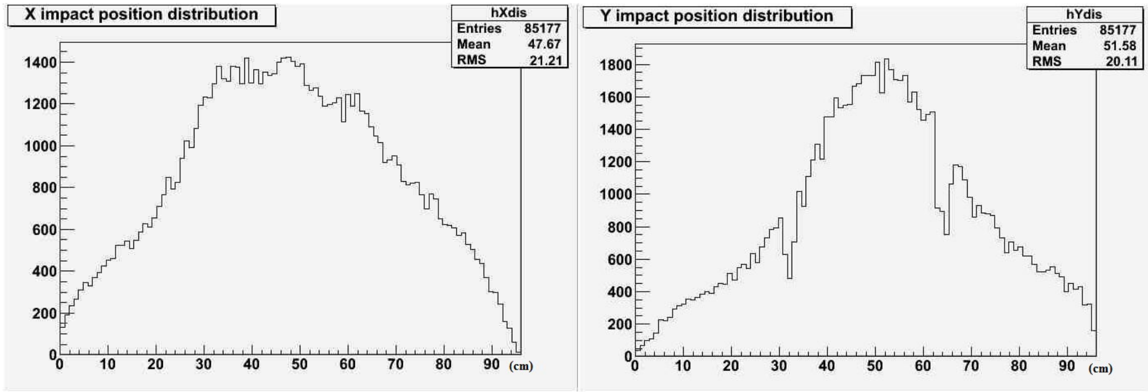

Figure 7.24: The X distribution (left) and Y distribution (right) of hits incident on the first layer of the DHCAL.

The y distribution is quite similar but has two additional features which are not seen in the x distribution. The two areas where the RPC frames make contact can be seen in the y distribution in Figure 7.24. The distribution of the y intercept with the front face of the detector is fitted with a Gaussian and has a mean of 52.4 cm and a standard deviation of 21.9 cm. Those values are to be used as input parameters for the simulation.

The last parameter needed for the input to Geant4 is the angle of incidence of the beam to the normal of the DHCAL. Figure 7.25 shows the angular distribution in degrees with an average angle of just less than 1 degree.

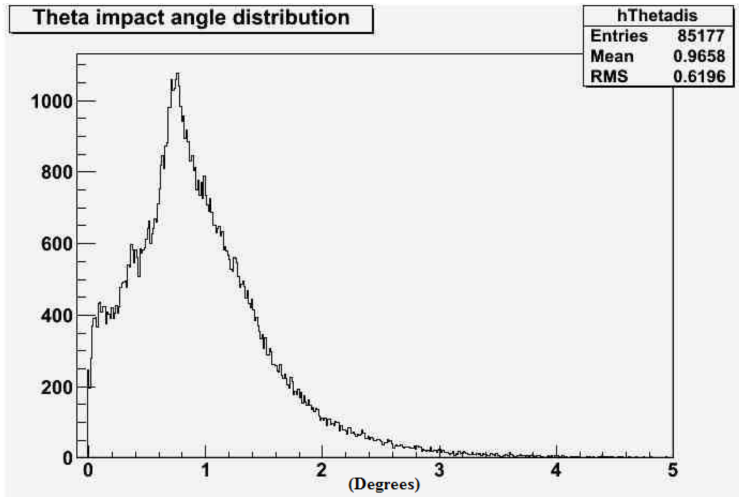

Figure 7.25: Histogram of the angle of incidence of each event on the front face of the DHCAL.

7.3.4 Alignment

The alignment of the DHCAL is not ensured by its design and has no physical mechanism to do it “perfectly”. A rough alignment of the cassettes are be made by hand and a ruler. This alignment is checked by using muons which typically leave straight tracks through the calorimeter. It is previously discussed how the residuals are calculated for each cluster in the event. The residuals information is now used to calculate the alignment of each of the FEBs. The alignment of each FEB is calculated since they may have moved relative to each other during the transport or cabling process. The residuals are calculated for the x and y dimensions separately, put into a histogram and then fitted with a Gaussian to get the mean values. Figure 7.26 shows the residual distributions for middle right hand FEB in the x dimension on layer 16.

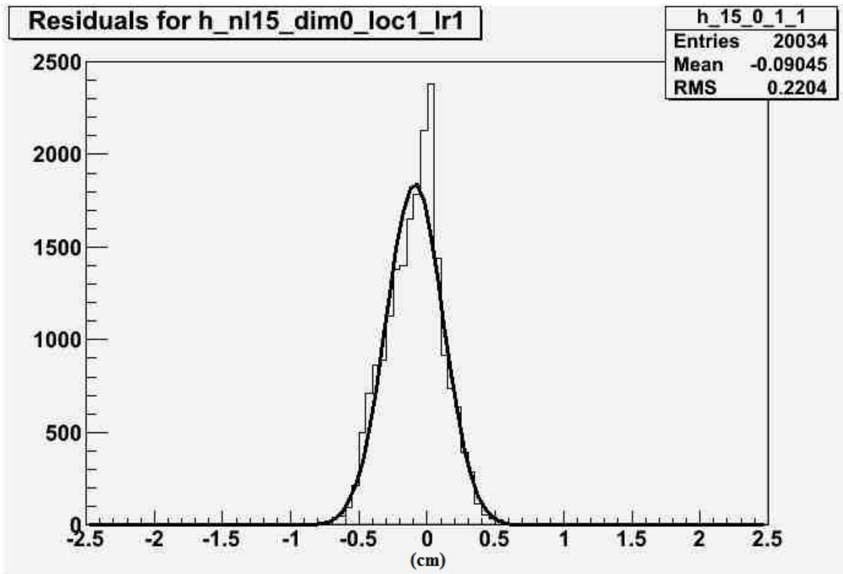

Figure 7.26: The residual profile for a single FEB fit to a Gaussian to find its mean and RMS.

It can be seen that the board is shifted to the left by approximately 1mm. The total of all the mean values are put together here to see the alignment as a whole of the DHCAL. Figure 7.27 shows the alignment of each of the 6 FEBs per layer of the DHCAL in the x dimension on the left and the y dimension on the right.

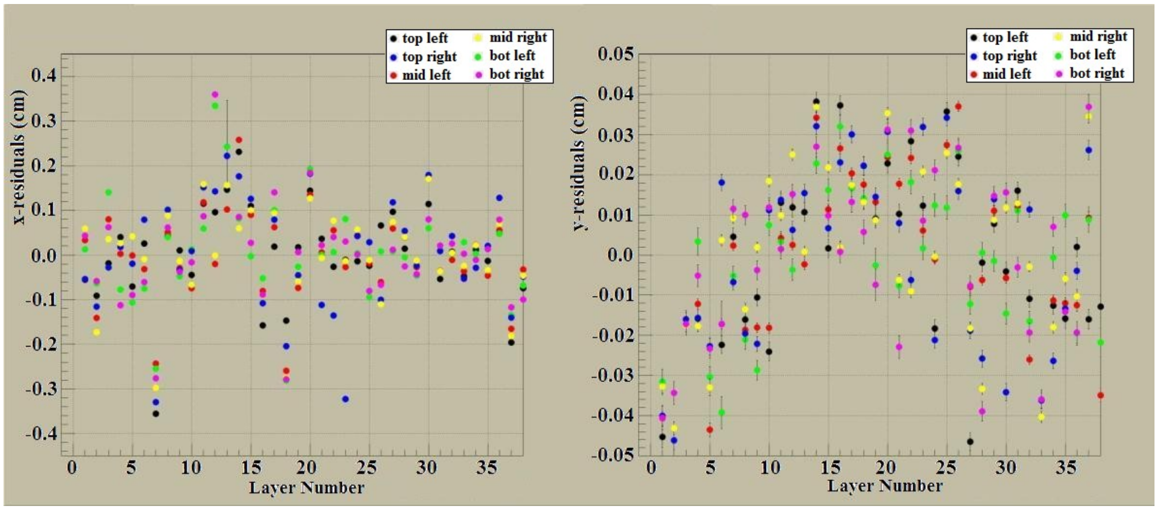

Figure 7.27: The residuals for each of the FEBs in the x direction (left) and y direction (right) calculated using all the tracks fit for a given run.

Figure 7.27 (right) demonstrates that the weight of the DHCAL is making the CALICE stage bow slightly in the middle. The residuals in the x dimension show a few boards that are relatively far out such as bottom right and left boards of layer 12. The projection of these two plots is used to give an overall sense of alignment, and is shown in Figure 7.28. The x distribution has a mean value of -0.0005 cm with an RMS of 0.24 cm and the y distribution has a mean value of -0.0001 cm with an RMS of 0.12 cm.

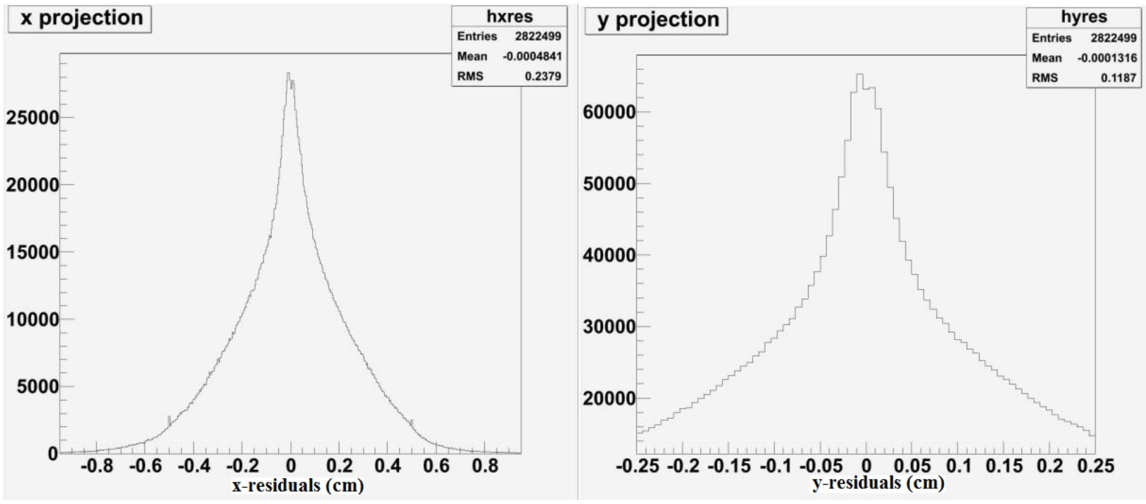

Figure 7.28: The X (left) and Y (right) projections of the residuals for all the FEBs.

The boards with a large misalignment are physically moved to aid with the alignment. After these alignments are calculated, the data is read in a second time. The hit positions are corrected by the misalignments of each FEB. To determine just how well this works the alignment is calculated a second time and Figure 7.28 displays the alignments for all the FEBs in the x and y dimensions separately.

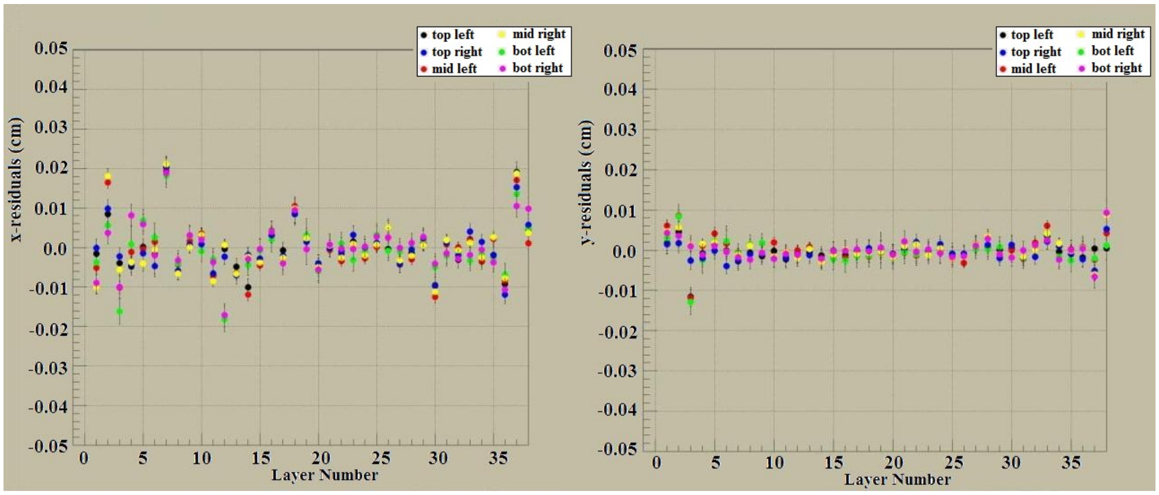

Figure 7.29: The residuals for each of the FEBs in the x direction (left) and y direction (right) calculated using all the tracks fit for a given run after alignment.

The alignments are roughly an order of magnitude better after the corrections. This shows that the alignment is working well. The projection of these is shown in Figure 7.30 which shows an overall improvement in the mean and an improvement in the RMS value.

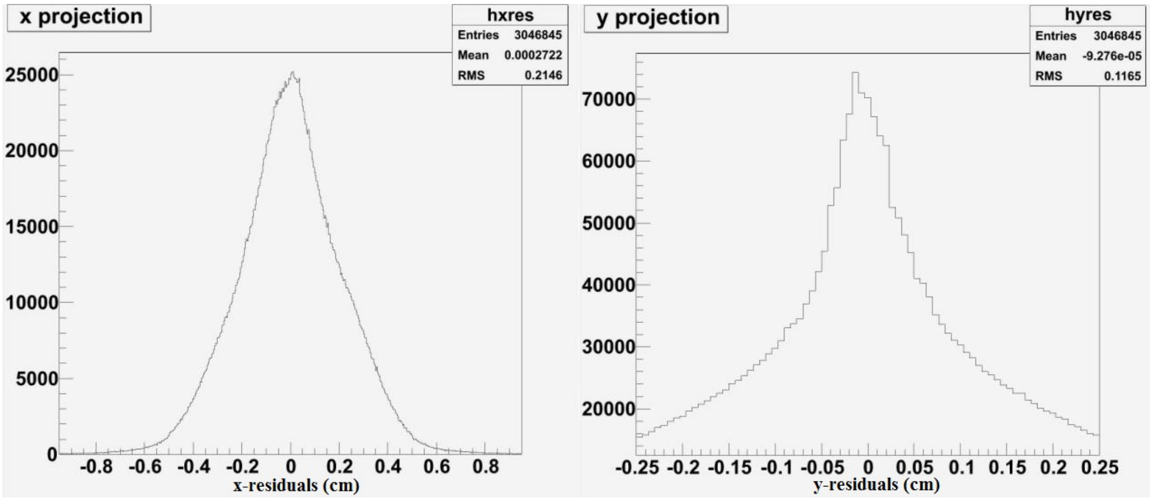

Figure 7.30: The residual projections of all the FEBs in the X (left) and Y (right) directions after software alignment.

The alignments calculated here are used in further analyses of all the runs granted nothing has been physically moved in the DHCAL (such as replacing a layer). The x distribution has a mean value of 0.0003 cm with an RMS of 0.22 cm and the y distribution has a mean value of -0.0001 cm with an RMS of 0.12 cm.

The alignments are used when looking at pion and positron tracks/showers. Hit to energy calibrations cannot be performed with the muons since the energy of the incident muons is not exactly known for each corresponding muon due to the nature of the muon energy loss. This hit to energy calibration will be performed with the momentum selected pions and positrons.

8 Discussions and Conclusion

Having calculated the efficiencies and multiplicities of each of the RPCs we can look for problem spots and either repair or replace the faulty RPCs. We can study the malfunctioning chambers to better understand these devices. The problems may be with the electronics boards and not the chambers themselves. All of these issues are important to study and understand if this technology is to be used in the future and be perfected.

An additional and important topic not discussed is the noise rate. This topic is large enough for a thesis by itself and so I will only make one comment. The noise rate is 0.2 Hz/pad as long as the DHCAL is kept at room temperature, as when the temperature increases the noise rate also increases.

The efficiencies and multiplicities calculated with muons are a good start to determine if the Monte Carlo simulations are working properly, i.e if our RPC response is simulated properly. As with any Monte Carlo simulation, if the results are correct then it’s possible that we understand the physics completely or that some of things we are doing wrong compensate to yield results that match the data. It requires lots of data and analysis to determine if it is the latter case and will only be done through further analysis.

It has been shown that RPCs are a technology to continue to pursue to determine their place in high energy physics. Work still needs to be done to calculate the energy resolution of such a device in order to determine its usefulness in the SiD detector design at the proposed ILC. The initial groundwork has been completed to allow for such an analysis to take place.

Bibliography

[1] A.White, The SiD Detector Concept, (2010), available from: http://arxiv.org/ftp/arxiv/papers/1006/1006.3503.pdf

[2] H. Aihara, P. Burrows and M. Oreglia, SiD Letter of Intent, (2009), available from: http://arxiv.org/PS_cache/arxiv/pdf/0911/0911.0006v1.pdf

[3] C. Amsler, T. DeGrand and B. Krusche, Particle Data Group, Particle Properties, Quarks, available from: http://pdg.lbl.gov/2011/reviews/rpp2011-rev-quark-model.pdf

[4] K. Hagiwara et al., Review of Particle Properties, Phys. Rev. D 66, (2002)

[5] G. Bernardi, M. Carena and T. Junk, Particle Data Group, Hypothetical Particles and Concepts, available from: http://pdg.lbl.gov/2011/reviews/rpp2011-rev-higgs-boson.pdf

[6] MissMJ, Standard Model of Elementary Particles, (2006), date retrieved: (2011), available from: http://en.wikipedia.org/wiki/File:Standard_Model_of_Elementary_Particles.svg

[7] S. Raby, Particle Data Group, Hypothetical Particles and Concepts, date retrieved: (2011), available from: http://pdg.lbl.gov/2011/reviews/rpp2011-rev-guts.pdf

[8] F. Zwicky, On the Masses of Nebulae and of Clusters of Nebulae, Astrophysical Journal 86:217, (1937)

[9] J. Brau et al., International Linear Collider Reference Design Report.1: Executive Summary. 2: Physics at the ILC. 3: Accelerator. 4: Detectors, (2007), ILC-REPORT-2007-001, available from: http://ilcdoc.linearcollider.org/record/6321/files/ILC_RDR_Volume_1-Executive_Summary.pdf?version=4

[10] C. Grupen and B.A. Schwatz, Particle Detectors, Cambridge University Press, pp. 19 (2008)

[11] K. Nakamura et al., Particle Data Group, J. Phys. G 37, 075021: 291 fig 27.10 (2010)

[12] C. Grupen and B.A. Schwartz, Particle Detectors, Cambridge University Press, pp. 21 (2008)

[13] J.S. Hubbell, H. Gimm, and I Overbo, Pair, triplet, and total atomic cross sections (and mass attentuation coefficients) for 1 MeV-100 GeV photons in elements Z=1 to 100, J. Phys. Chem. Ref. Data, 9, 1023 (1980).

[14] D.E. Groom, N.V Makhov and S.I. Striganov, Muon stopping-power and range tables: 10 MeV-100 TeV, Atomic Data and Nuclear Data tables, 78, 183-356 (2001).

[15] ICRU, Stopping Powers and Ranges for Protons and Alpha Particles, ICRU Report No. 49 (1993), available from http://physics.nist.gov/PhysRefData/

[16] I. C. Brock, Simple shower model, date retrieved: (2011), available from: http://www-zeus.physik.uni-bonn.de/~brock/feynman/vtp_ws0506/

[17] W.R Nelson, H. Hirayama, and D.W.O. Rogers, The EGS4 Code System, SLAC-265, Stanford Linear Accelerator Center (1985).

[18] M. J. Berger and S. M. Seltzer, Tables of Energy Losses and Ranges of Electrons and Positrons, National Aeronautics and Space Administration Report NASA-SP-3012 (Washington DC 1964).

[19] E. Longo and I. Sestili, Monte Carlo calculation of photon-initiated electromagnetic showers in lead glass, Nucl. Instrum. Methods 128, 283 (1975)

[20] W. R. Nelson et al., Electron-Induced Cascade Showers in Copper and Lead at 1 GeV, Phys. Rev. 149, 201 (1966)

[21] G. Bathow et al., Measurements of the longitudinal and lateral development of electromagnetic cascades in lead, copper and aluminum at 6 GeV, Nucl. Phys. B20, 592 (1970)

[22] G. Grindhammer et al., Proceedings of the Workshop on Calorimetry for the Supercollider, Tuscaloose, AL, March 13-17, 1989, edited by R. Donaldson and M.G.D. Gilchriese (World Scientific, Teaneck, NJ, 1989), p. 151.

[23] C. W. Fabjan and T. Ludlam, Calorimetry in High-Energy Physics, Ann. Rev. Nucl. Part. Sci. 32 (1982), reprinted in Formulae and Methods in Experimental Data Evaluation, R.K. Bock ed., European Physical Society (1984).

[24] M. Thomson, Particle Flow Calorimetry and Pandora PFA, date retrieved: (2011), available from: http://www.desy.de/dvsem/SS08/thomson_talk.pdf

[25] Mary-Cruz Fouz, R&D on Calorimetry for the ILC inside the CALICE Collaboration, date retrieved: (2011) available from: http://indico.ific.uv.es/indico/getFile.py/access?contribId=14&resId=0&materialId=slides&confId=121

[26] J.C. Brient et al., CALICE Report to the Calorimeter R&D Review Panel, (2007). arXiv:0707.1245

[27] R. Cornat, Semiconductor sensors for the CALICE SiW EMC and study of the cross-talk between guard rings and pixels in the CALICE SiW prototype, Journal of Physics: Conference Series 160 (2009) 012067

[28] The CALICE Collaboration, Preliminary results from hadron shower data with the CALICE tile AHCAL prototype, CALICE Analysis Note-003, (June 16, 2007)

[29] The CALICE Collaboration, Preliminary study of the combined response of the CALICE calorimeter prototypes to pion beams, CALICE Analysis Note-004 (June 29, 2007)

[30] R. Santonico and R. Cardarelli, Development of Resistive Plate Counters, Nucl. Instr. Meth., 187, pp. 377-380, (1981)

[31] G. Drake and J. Repond, DHCAL Electronics Production Summary, CALICE Meeting – CERN, page 14, (2011)

[32] B.Bilki et al., Measurement of the rate capability of Resistive Plate Chambers, pp. 3-5, (2009), available from: http://iopscience.iop.org/1748-0221/4/06/P06003/pdf/1748-0221_4_06_P06003.pdf

[33] S. Agostinelli et al., Geant4 – a simulation toolkit, Nuclear Instruments and Methods in Physics Research A 506 (2003), pp.250-303